AIR FORCE INSTITUTE OF TECHNOLOGY

LEVEL

AIR UNIVERSITY
UNITED STATES AIR FORCE
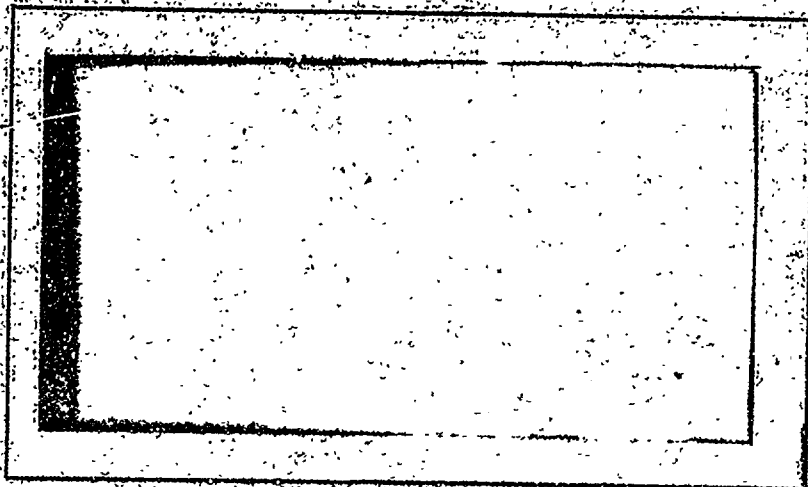
D D C

RECEIVED

FEB 5 1980

A

SCHOOL OF ENGINEERING

WRIGHT-PATTERSON AIR FORCE BASE, OHIO

MEASUREMENTS ON ELECTRON IMPACT EXCITATION

FUNCTIONS OF XENON TRANSITIONS.

Master's THESIS

AFIT/GEP/PH/79D-11   MARK D. STEPHEN
                                            2nd Lt   USAF

Dec 79   89

Approved for public release; distribution unlimited.

012 225

LB

MEASUREMENTS ON ELECTRON IMPACT EXCITATION

FUNCTIONS OF XENON TRANSITIONS

THESIS

Presented to the Faculty of the School of

Engineering of the Air Force Institute of Technology

Air University

in Partial Fulfillment of the

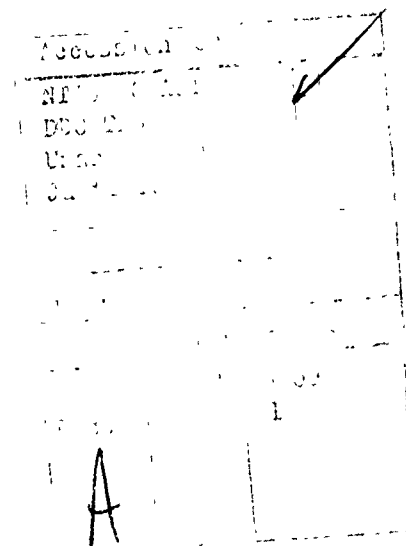Requirements for the Degree of

Master of Science

by

Mark D. Stephen, B.S.

2nd Lt.   USAF

Graduate Engineering Physics

December 1979

Approved for public release; distribution unlimited.

Preface

Deep appreciation is given to Cliff Vansickle for production of the electron gun and to Vivian E. Merchant for his help in the standardization procedure.

Special thanks is given to Max L. Lake for pulling me through despite my problems and to Alan Garscadden for pushing me through the thesis.

The author is extremely grateful to Joy Williams for her excellent typing abilities.

A large measure of profound gratitude is due my wife, Anne, for her patience and inspiration during the course of this work.

Table of Contents

List of Figures

List of Symbols

N	Number density of the gas
A	Area of the electron beam
ℓ	Length of the interaction volume
Q_i	Cross sections in cm^2 of each atom in the area A
N_e	Electron number density
v_e	Electron velocity
$\sum_j F_{ij}$	De-excitation from i^{th} state
$\sum_k F_{ki}$	Cascading into i^{th} state
ΔX	Width of Observation slit
d	Diameter of electron beam
H	Height of the observational volume
F_{ij}	Photon flux for one transition
I	Electron current
e	Electron charge
A_{ij}	Einstein coefficient for spontaneous emission from i to j
B_{ij}	Branching factor for i to j transition
Q_{ij}	Optical cross section
Ω	Solid angle
$F_{ij}(\Omega)$	Photon flux in certain solid angle
$S(\lambda)$	Spectrum Sensitivity
$t(\lambda)$	Transmission factor
I_c	Detector signal
N_s	Total current density of electrons

Symbols

m	Mass of electrons
v	Electron velocity
K	Boltzmann's constant
T	Temperature in degrees Kelvin
E	Energy
V_r	Retarding potential
π	3.14159
R	Lens radius
S_o	Object distance
t_m	Monochromator transmission factor
λ	Wavelength
λ_o	Wavelength for peak transmission
$\Delta\lambda$	Monochromator bandpass
t_w	Transmission factor of chamber window
t_L	Transmission factor of standard lamp window
P	Spectral radiant flux
R	Spectral reflectance
N	Spectral of radiance
S	Area of spectrometer slit
A	Area of limiting optic
D	Distance of optic from slit
A_S	Area of tungsten ribbon
Ω_S	Solid angle for standardization
t_s	Transmission factor of standar lamp window
$R_N(\lambda,T)$	Photon radiancy

Symbols

F_S	Photon flux
$e(\lambda, T)$	Emissivity of tungsten ribbon
$R_N^B(\lambda, T)$	Blackbody photon radiancy
h	Plank's constant
C	Speed of light
C_1	Constant
C_2	Constant
ψ_i	Wave function for particle
k_i	Wave number for particle
θ	Angle of incidence

Abstract

Electronic impact excitation functions were measured for xenon in
a pressure region in the 10^{-4} torr range. A one centimeter diameter
electron beam was used to excite the gas atoms. The electron gun pro-
duced a current of approximately one milliamp. Measurements were made
in the regions where the signal was linearly proportional to current and
pressure.

Most of the xenon I cross sections were sharply peaked around 18
eV. Broader excitation functions were measured which had peak cross
sections at electron energies around 30 eV. Cascading from higher
energy levels showed significant effects on selected optical excitation
functions.

Conditions enabled measurement of xenon II lines produced by
simultaneous ionization/excitation. The xenon II excitation functions
demonstrated a maximum at approximately 35 eV, and a broader shape than
the Xe I 5s→6p excitation functions.

I. INTRODUCTION

Interaction between an electron beam and a volume of gas may lead to inelastic collisions such as ionization or excitation of the gas atoms. The probability that a given atom will exhibit a specific reaction due to a collision with a specific kind of incident particle and its energy can be formulated using a classical construct termed the cross section. Atomic or molecular cross sections for excitation to bound states can be determined by examining the wavelengths of light emitted after the interaction has occurred. Cross sections as a function of the bombardment energy are termed excitation functions and such data for specific lines are useful as a basis for development of lasing predictions for certain gases. They can also be used to determine the utility of a gas as a particular wavelength source. Cross sections are also needed for theoretical analysis of astrophysical phenomena.

Optical cross sections for excitation to states that radiate in visible regions of the spectrum have been measured for many of the noble gases. However, measurements of excitation cross sections for transitions with wavelengths in the infrared region are needed. These transitions have long wavelengths, typically 2-5μm. The infrared transitions are important in lasing applications. This experiment is necessary to complement the theoretical modeling and enhance knowledge of interactions in this region of study. Observations of xenon gas have shown that strong lasing lines exist for transitions which origi-nate on all 5d levels and terminate on one of the 6p levels (refer to arrow in Figure 1). Electron collision is apparently the primary means of excitation (Ref. 1:39) and thus, this experiment has been devised to examine some of these transitions.

1
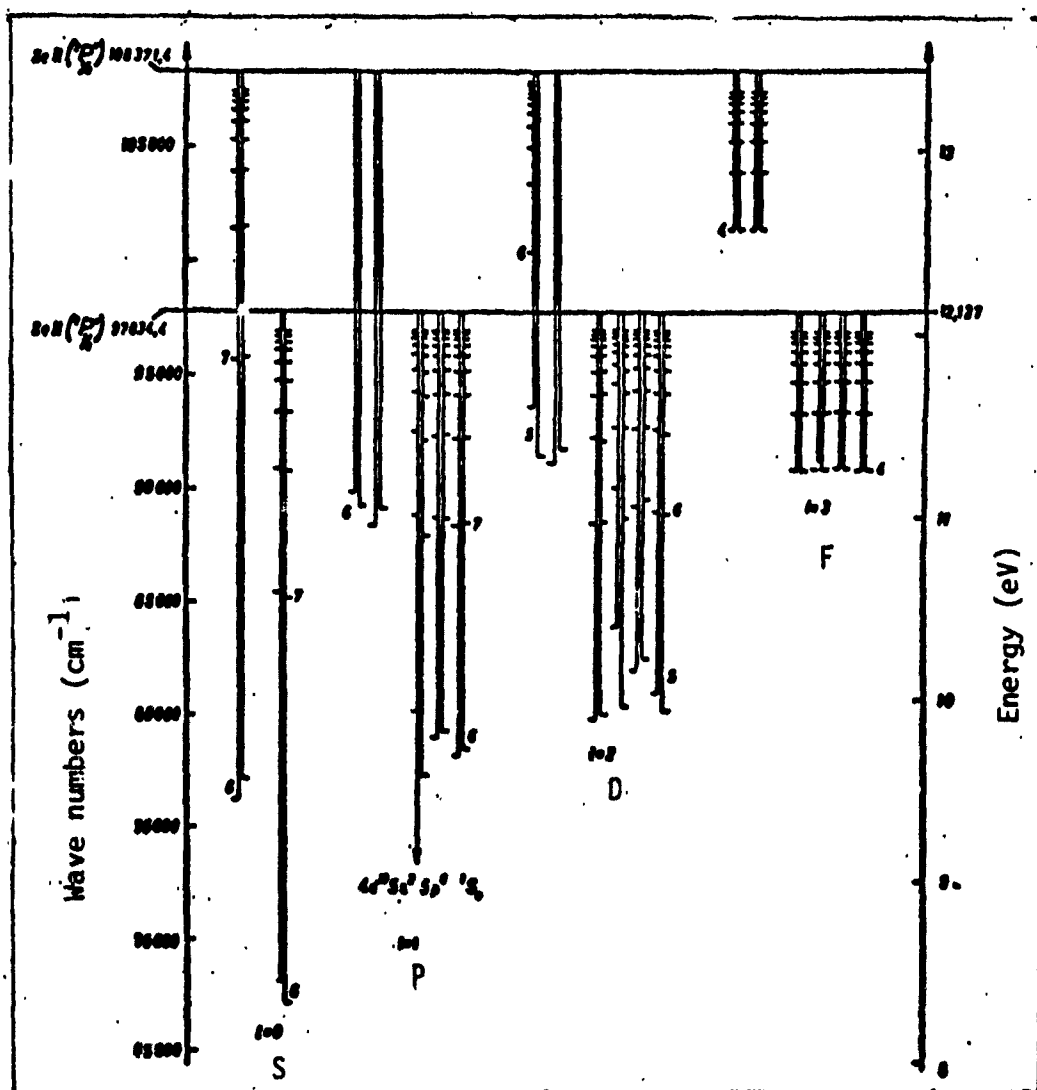
Figure 1.   Energy Level Diagram of Xenon (Ref. 2).

II. EXPERIMENTAL PROCEDURE

Rate Equation

The equation describing the rate of population of the ith state of the gas from electron impact is given by:

$$\frac{dN}{dt} = NA\ell \frac{Q_i}{A} \int N_e v_e \, dA' + \Sigma F_{ki} - \Sigma F_{ij} \pm \text{collisional} \quad (1)$$
$$\text{terms}$$

where N is the number density of the gas, A is the area of the electron beam, ℓ is the length of the interaction volume, Q_i is the cross section in cm^2 of each atom in the area, N_e is the electron number density, v_e is the electron velocity, $\Sigma_k F_{ki}$ denotes cascading into the ith state, and $\Sigma_j F_{ij}$ denotes excitation from the ith state (Ref. 3). Figure 2 shows the relative positions of levels i, j, and k. The interaction volume is the region of interaction between the electron beam and the gas. The interaction volume is well defined if it is assumed that the gas atoms are stationary compared to the electron velocity. The target chamber is filled with the target gas. Electron-electron collisions and charge repulsion in the interaction volume result in enlargement of the electron beam diameter, giving the beam a conical shape as shown in Figure 3. To account for this divergence, the observational volume must include all of the electron beam.

The observational volume is the region of the interaction volume from which radiation is collected. The two volumes are shown in Figure 3. The interaction volume is denoted by $A\ell$ where A is the area of the electron beam at the center of the electron observational slit and ℓ is the length of the target chamber. The observational volume is ΔxHd where

3
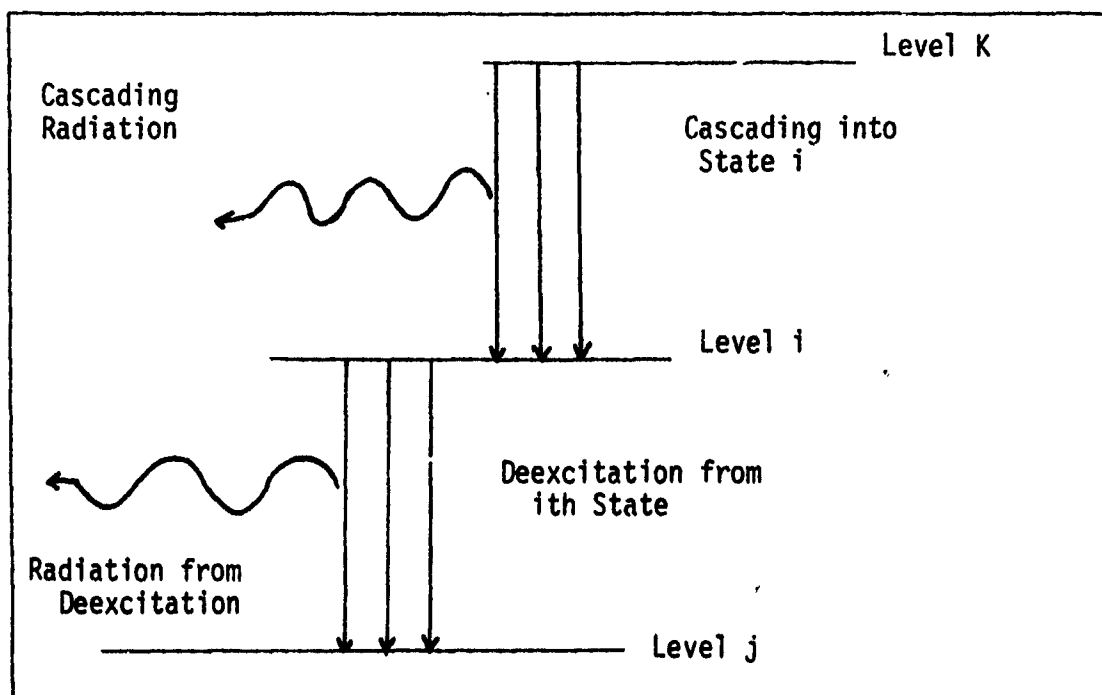
Figure 2. Relative Energy Levels.

Δx is the width of the observation slit, H is its height, and d is the
diameter of the electron beam, assumed rotationally symmetric. The
height, H, of the observational volume must be greater than the diameter,
d, of the electron beam. This accounts for the divergence of the beam
through the target chamber; and accomodates non-uniform current density
as a function of electron velocity.

Cross Section Formula

The rate equation, Equation (1), can now be used to solve for the
cross section, Q. At low pressure, less than 10^{-3} torr, the collisional
transfer term can be neglected because experiments (Ref. 3) have shown
these not to be significant in the population scheme. After electron
impact excitation for a sufficient period of time, depending on the

4
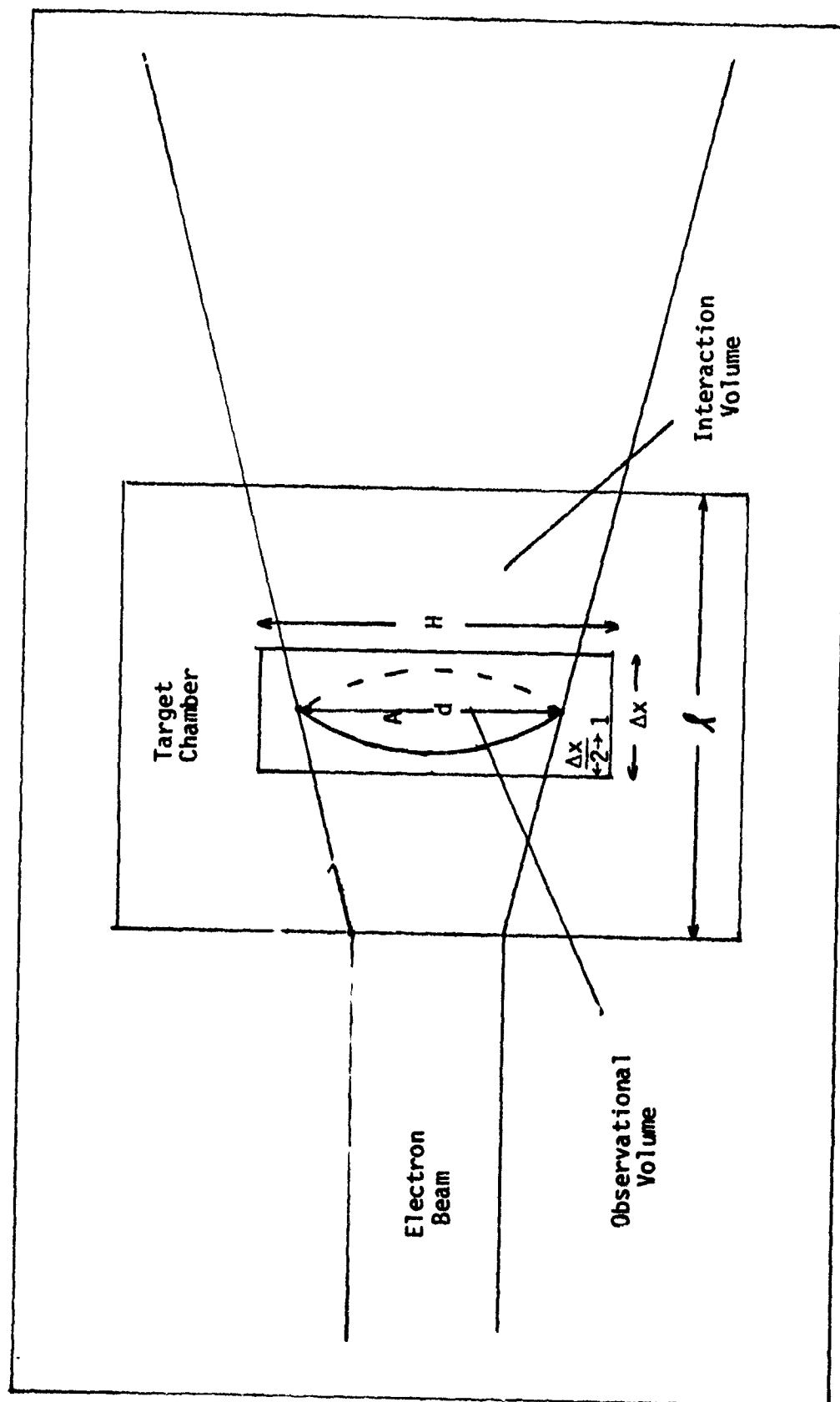
Figure 3. Interaction/Observational Volume.

lifetime of the observed state, the rate of change of the number of atoms in the ith state goes to zero. Solving for the cross section of the ith state gives:

$$Q_i = \frac{\sum\limits_{j} F_{ij} - \sum\limits_{k} F_{ki}}{N\ell \int_A N_e v_e dA'} \quad . \tag{2}$$

This is termed the level cross section for the ith state. The level cross section concerns all transitions out of a particular level and deletes cascade contributions. The optical cross section for a particular transition is given as:

$$Q_i = \frac{F_{ij}}{N\ell \int_A N_e v_e dA'} \quad , \tag{3}$$

where F_{ij} is the photon flux for one transition. The optical cross section includes only the photon flux for a particular transition and has no cascade considerations. The photon flux can be measured by setting the monochromator to a specific transition wavelength.

It is necessary to express the cross section in terms of laboratory parameters. Once a workable formula has been derived, the cross section can be calculated for different electron energies. A curve which represents the cross section for state i as a function of electron energy is known as the excitation function for state i. The level cross section for the ith state, Q_i, is given in square centimeters and is dependent on the energy of impacting electrons.

6

In the target chamber, the number of electrons per second which will suffer a collision with an atom in which that atom will end up in state i is $N\ell Q_i \int_A N_e v_e dA'$ where $\int_A N_e v_e dA'$ is the number of electrons passing through A each second. The current I can be expressed as,

$$I = e \int_A N_e v_e dA' \quad . \tag{4}$$

Substitution gives the number of electrons per second suffering appropriate collisions as $N Q_i I/e$. Replacing ℓ by Δx (because only radiation from the smaller region will be observed) and summing the photon flux yields:

$$N \Delta x Q_i I/e = \sum_j F_{ij} - \sum_k F_{ki} \quad . \tag{5}$$

However, it is difficult to include all lines for transitions into and out of the ith state. The photon flux for the transitions from state i to state j can be expressed as (Ref. 4:12),

$$F_{ij} = A_{ij} \int N_i A' dx \quad , \tag{6}$$

where A_{ij} is the Einstein coefficient for spontaneous emission from i to j, and the integral is over the observational length of the electron beam. The total photon flux for all such transitions is

$$\sum_\ell F_i = \sum_\ell A_{i_\ell} \int N_i A' dx \quad . \tag{7}$$

Combining the above two equations yields,

7

$$\sum_\ell F_i = \frac{\sum_\ell A_{i\ell}}{A_{ij}} \; F_{ij} \; . \tag{8}$$

The term $\sum_\ell A_{i\ell}/A_{ij}$ is called the branching factor of the i to j transition and can be denoted by B_{ij}. The total flux can be obtained by measuring the photon flux for one transition and by using the appropriate branching factor. Equation (5) then becomes:

$$N\Delta x Q_i I/e = F_{ij}/B_{ij} - \sum_k F_{ki} \; . \tag{9}$$

This can be rewritten to give an expression for the direct cross section:

$$Q_i = \frac{1}{B_{ij}} \frac{F_{ij}}{N\Delta x I/e} - \sum_k \frac{F_{ki}}{N\Delta x I/e} \; . \tag{10}$$

The cross section for a specific transition can be defined as,

$$Q_{ij} = \frac{e(F_{ij})}{N\Delta x I} \; , \tag{11}$$

which is identical to Equation (3). Equation (11) is the optical cross section of the spectral line due to the transition from state i to state j. Substituting this into Equation (10) yields,

$$Q_i = \frac{Q_{ij}}{B_{ij}} - \sum_k Q_{ki} \; . \tag{12}$$

The term Q_{ij}/B_{ij} is the apparent cross section of level i. It should be noted that branching factors are often sensitive to the scheme of generation and should be avoided when possible by determining the total cross section with actual measured sums of optical cross sections (Ref. 4:14).

8

Calculation of cross sections by use of photon flux is also troublesome because photon fluxes are difficult to measure. The detection system will measure radiation in a particular solid angle from the observation region:

$$F_{ij} = \frac{4\pi}{\Omega} F_{ij}(\Omega) \quad .$$ (13)

In Equation (13), $F_{ij}(\Omega)$ is the photon flux gathered in a certain solid angle Ω. It will be assumed that the emitted radiation is isotropic. This is not always the case, but it simplifies the equation by disregarding polarization effects, which are negligible in many cases (Ref. 4:13). The detection system will measure a signal which is proportional to $F_{ij}(\Omega)$. The proportionality constant will include spectral sensitivity of the detection devices, $S(\lambda)$; and the transmission factors of various optical components, $t(\lambda)$ (Ref. 4:14).

$$I_c = t(\lambda)S(\lambda)F_{ij}(\Omega) \quad .$$ (14)

The signal displayed by the detector is denoted by I_c. From Equations (11), (13), and (14) it can be shown that

$$Q_{ij} = \frac{4\pi \ e \ I_c}{\Omega N \Delta x t(\lambda)S(\lambda)I} \quad .$$ (15)

This defines the cross section in terms of known or measurable quantities. The spectral sensitivity can be determined from a known source.

9

III. APPARATUS

Vacuum System

The vacuum system was capable of reaching pressures as low as 10^{-7} torr. All accessible tubes were wrapped with heating tape to enhance outgassing of the system during the bake out cycle. The actual pumping was accomplished by use of a mechanical forepump in series with a Welch turbo-molecular pump. The turbo-molecular pump was a model 3103 which has a pumping speed of 140 liters per second. The pressure was measured by a Baird Alpert nude gauge and a Baratron capacitcance manometer. The manometer measured relative pressures between a reference getter-pumped volume and the system. All flanges had copper gaskets and the gate valve used O-rings. The gate valve was set to close automatically should the line voltage drop. This prevented contamination of the major sections of the system due to oil backstreaming from the pumps when they stopped pumping. The vacuum system is diagrammed in Figure 4 (Ref. 5).

For pressure calibration, the flow of gas in the system was stopped when the target chamber had been filled. This eliminated the need for flow equations and non-uniformity calculations on the gas. However, static conditions create danger of cathode contamination by residual oxygen. Therefore, a Saes Sorb-AC AP-ION appendage pump was used. This pump was operated at 0.6 amps and 30 volts to yield a pumping speed for oxygen of 9.2 liters per second, but did not pump the rare gas effectively.
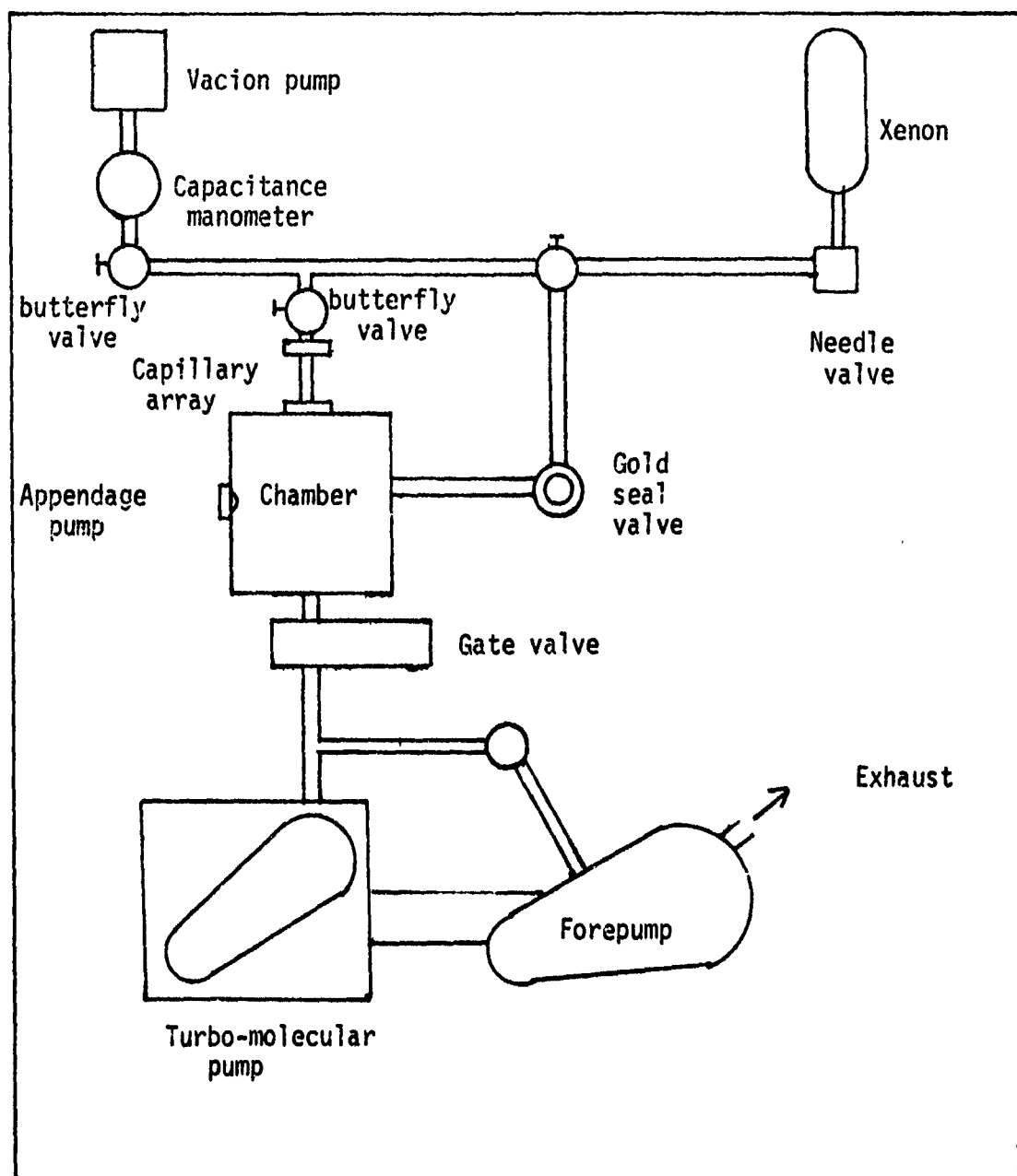
Figure 4. Vacuum System.

Electron Gun

A monoenergetic electron beam is desirable during the direct excitation of the gas atoms. However, it is difficult to produce a perfectly monoenergetic electron beam. The retarding-potential-difference method described later in this section will produce a narrow electron energy distribution. For the present application, an excited

11

state density of 10^8/cc out of a total density less than 10^{14} is accep-
table.

The electron gun produced a one centimeter diameter electron beam
to increase the observable interaction-volume and ensure adequate
signal. Therefore, the signal to noise ratio was increased and the
amount of possible error was decreased. The emitter was composed of
porous tungsten impregnated with barium. It was heated to 1050° K and
thus because an IR emitter. It was necessary to shield the detector
to prevent this radiation from reaching the detection system; so the gun
was housed in a cylindrical copper shield (refer to Appendix C). The
shield was 3.75 inches in length and 3 inches in diameter. A 1/16 inch
observation slit was cut in one side of the shield (see Figure 3). The
opposite side included a 3/16 inch slit to prevent radiation reflection.
Alcohol flowing through a coil around the housing cooled it to approxi-
mately -20°C (Ref. 6). The gun housing and cooling coil were electro-
polished to remove sharp edges or scratches in the metallic surfaces
which could trap contaminants. The electron beam was defined by a
series of five grids spaced 0.050 inches apart. The grids are centered
in stainless steel discs which are connected by precision-ground alumina
sleeves. This technique was developed by C. K. Crawford (Ref. 7:128).
The grids are made of 0.25 mm thick molybdenum mesh. A typical disc is
drawn in Figure 5.

The discs are 0.020 inches thick and 5 cm in diameter. Stainless
steel clips placed around the alumina rods ensured that the grids would
not slide or separate. Tungsten springs were used to allow room for
the components to spread when heated so as not to touch one another.
Pyrex sheaths surrounded the alumina rods in the interaction region to

12
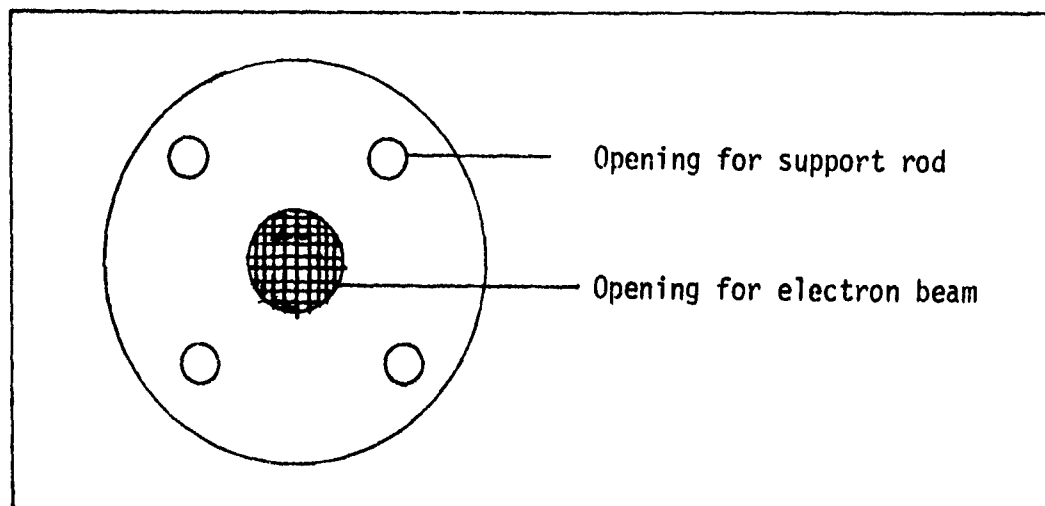
Figure 5. Electron Gun Grids.

prevent absorption of the radiation and to separate the grids. Alumina spacers were used to separate the other discs.

The electron gun described in the previous paragraphs was operated using a modulation technique which is capable of embracing the retarding-potential-difference (RPD) method. The RPD method was originally designed by R. E. Fox, W. M. Hickam, T. Kjeldaas Jr., and D. J. Grove (Ref. 8:859). The technique involved maintaining the intermediate electrode at a negative potential with respect to the cathode which prevented low energy electrons in the distribution from entering the target chamber. The retarding potential V_r was applied directly to a disc in the path of the electron beam. The adjacent slits were kept at a potential close to V_r to provide a uniform potential in the plane of the retarding disc.

The RPD method was revised in 1959 by G. G. Cloutier and H. I. Schiff (Ref. 9:473). They used a potential minimum in the region between the filament and the anode to produce the retarding potential.

The initial energy distribution of electrons can be calculated from Maxwell's equations. The number of electrons dN_s emitted per unit area per unit time which have velocities between v and v + dv is (Ref. 9:475):

$$dN_s = N_s \frac{mv}{kT} \quad \exp \quad -\left[\frac{mv^2}{2kT}\right] dv \quad , \tag{16}$$

where N_s is the total current density of electrons leaving the filament, m is the mass of the electrons in kilograms, v is the electron velocity in m/sec, k is Boltzmann's constant, and T is the temperature in degrees Kelvin. By making use of the fact that $E = \frac{1}{2}mv^2$ and the differential dE = mvdv, the number dN_s can be converted to terms of energy. Equation (16) becomes,

$$dN_s = \frac{N_s}{kT} \quad \exp \left[\frac{-E}{kT}\right] \quad dE \quad , \tag{17}$$

which represents the number of electrons emitted from the filament per unit area per unit time with energies between E and E + dE. A graph of the exponential distribution is shown in Figure 6.
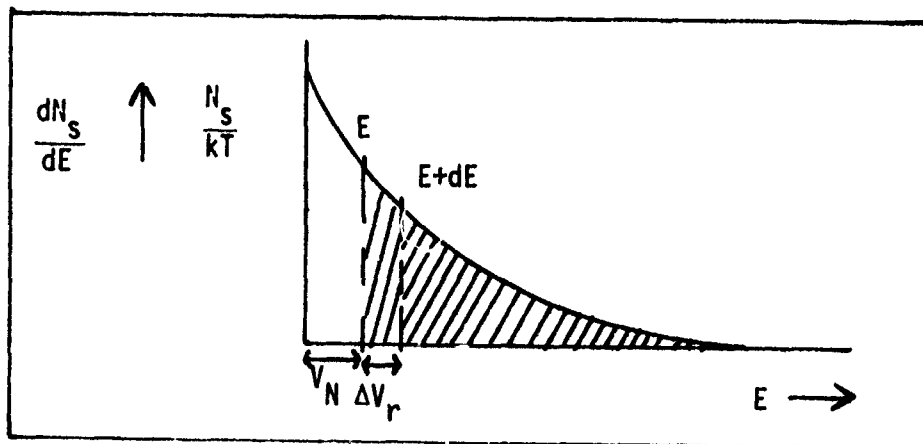
Figure 6.   Electron Distribution (Ref. 9:477).

The electrons to the right of V_r have sufficient energy to surmount the potential barrier, but retain the same distribution.

Resulting from the need for large signals, energy resolution obtainable from the RPD method was traded for high currents obtained using a simple modulation technique. The arrangement used to obtain the desired electron currents is shown in Figure 7. Element A is the
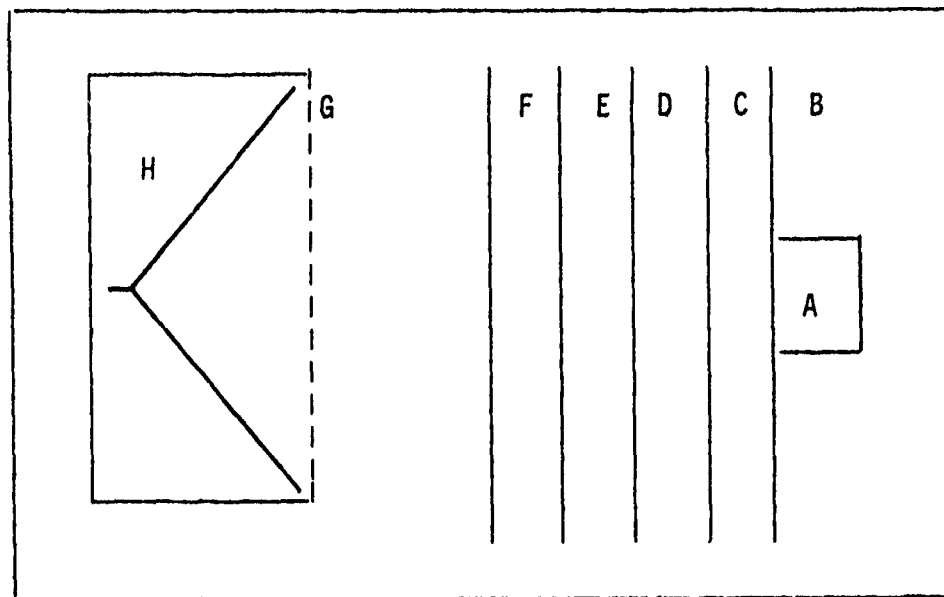
Figure 7.   Electron Gun.

cathode to which the heater current is applied; element B is termed the Accel and has the accelerating voltage applied to it. Element C is the anode and is modulated from zero to a positive voltage with respect to the cathode so that the current is biased off during one half cycle. Element D is termed the grid and is also negative with respect to the cathode; element F is termed the chamber and is at ground potential; element G is a Faraday cage and is also at ground potential; element H is the collector to which the cup voltage is applied. The distance from the Faraday cage to the Chamber is 0.6 inches. Element E insures

15

that the electrons have an energy at least as great as those leaving the cathode. The region between elements F and G is essentially field-free. The interaction volume is located in this region.

The wiring used to achieve the desired potentials is shown in Figure 8. Wires were fed through the faceplate (see Figure 9) inside alumina insulators and excited the chamber through a twenty pin connector. The pins of the connector were labeled alphabetically to eliminate cross wiring. The faceplate was made of 0.030 inch thick copper and was 9 cm in diameter. It was attached to the copper cooling shield by the support rod and shield connections.
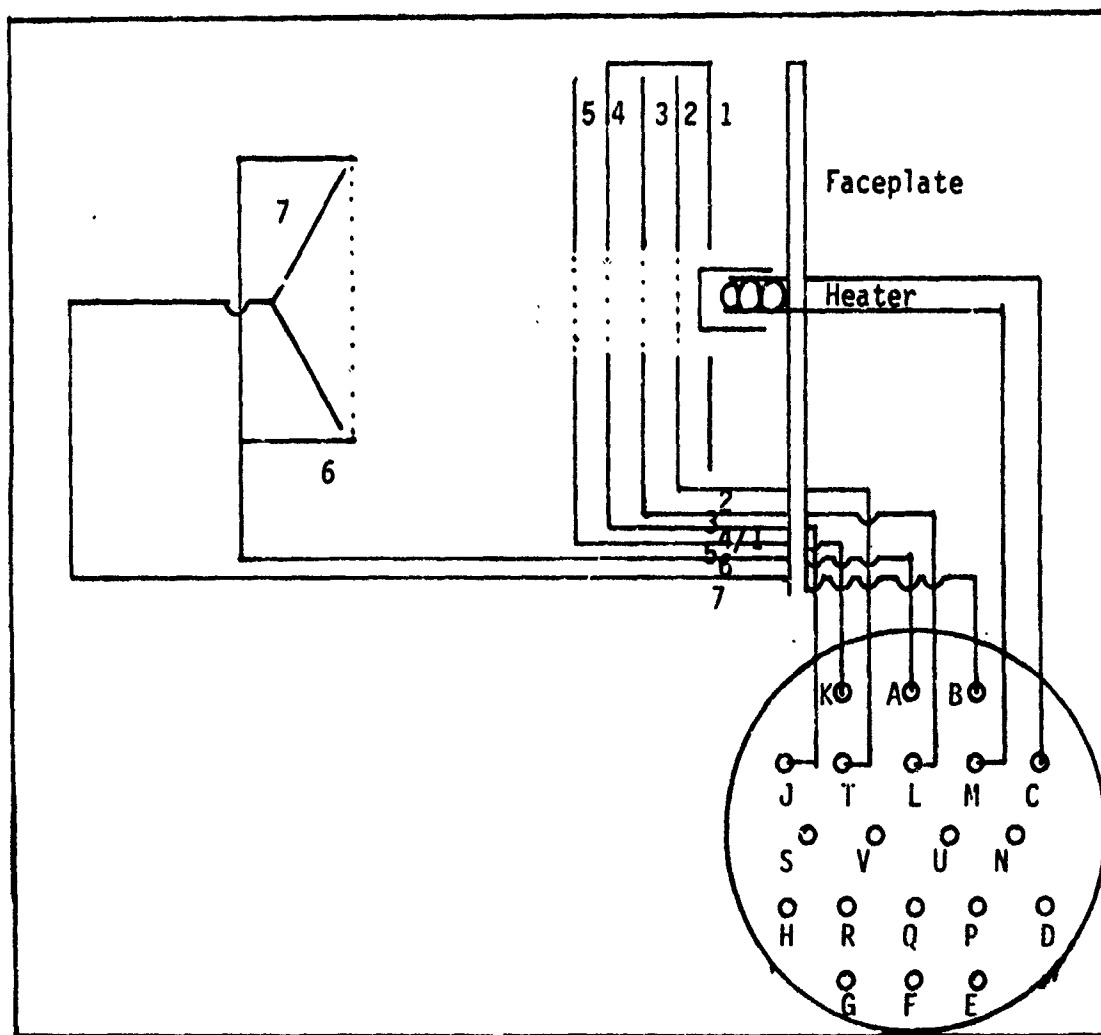
Figure 8.   Electron Gun Wiring.
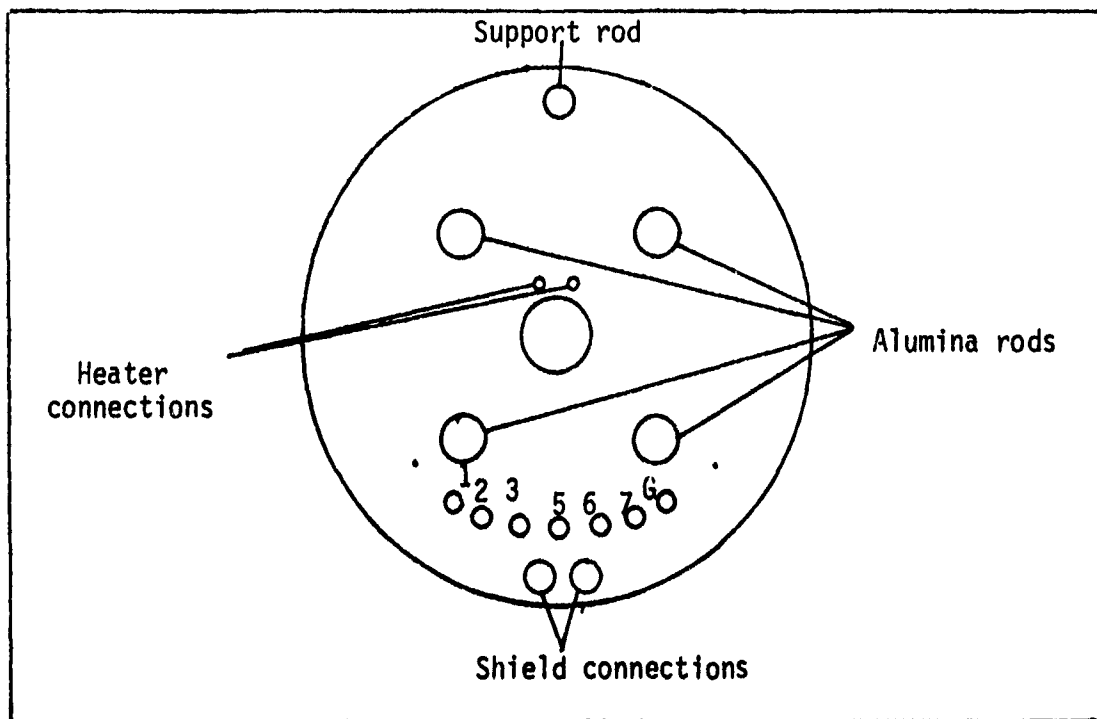
Figure 9. Copper Shield Faceplate.

Figure 10 shows the wiring connections through a patch panel and into the power supply. The power supply used was designed by P. Bletzinger and built by P. D. Tannen (Ref. 10). An external accelerating voltage was drawn from a Fluke power supply, model 330B. Photographs of the electron gun are shown in Appendix B.

Detection System

The detection system included a lens to focus the emitted radiation, a monochromator, and a detector. While measuring excitation functions of visible and near IR lines, a fused quartz lens with a focal length of 10.15 cm was used. A half-meter Jarrel-Ash monochromator was used to select the chosen wavelength with a two inch square grating of 560 lines/mm giving a resolving power of 89916. The grating was blazed at 6000 $\overset{o}{A}$. An RCA photomultiplier model 31034A detected the photons in
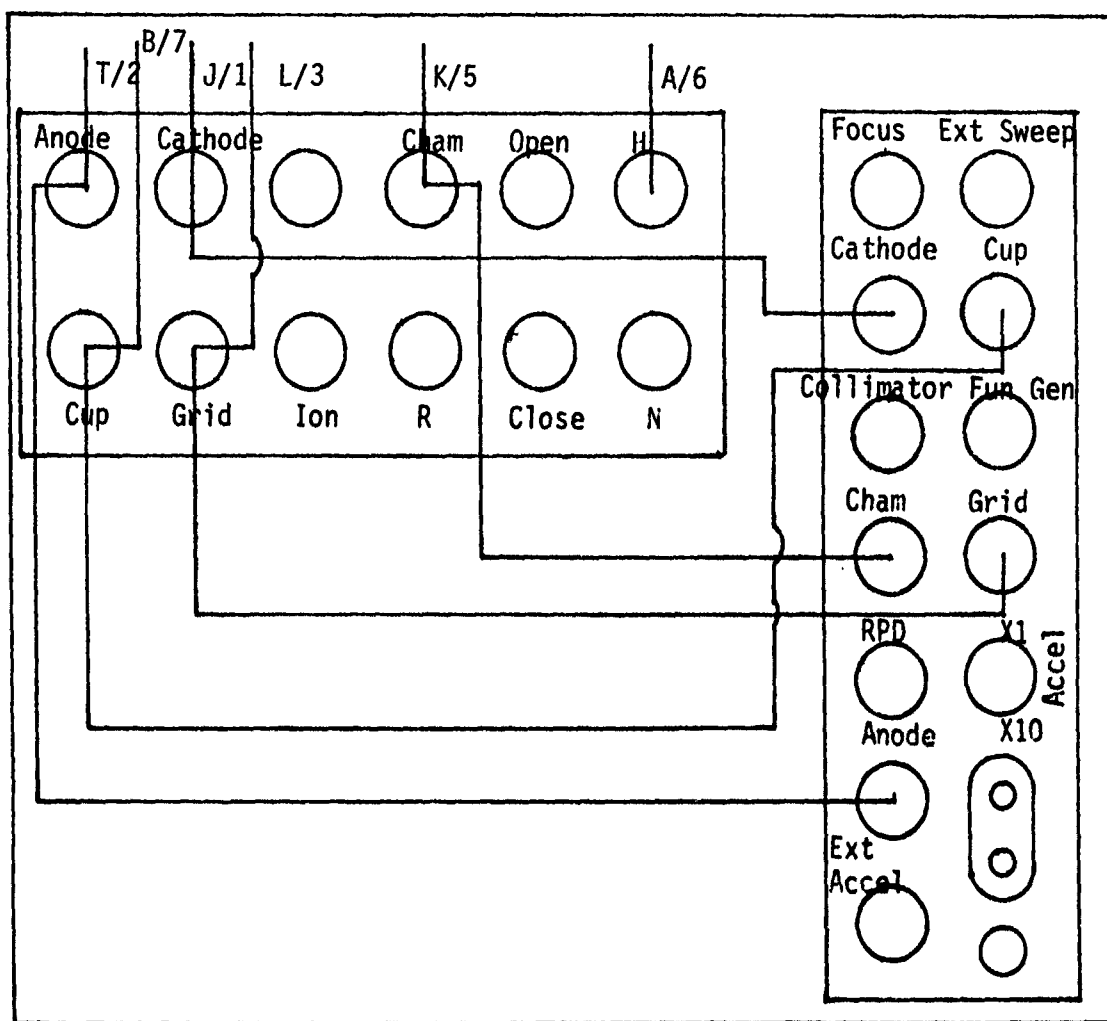
Figure 10. Patchpanel to Power Supply.

the 3000-9000 $\overset{o}{A}$ region. The spectral sensitivity as a function of wave-
length of the detection system is plotted in Figure 11. The PMT was
biased at 1500 V and thermoelectrically cooled to -20^0C by a refrigera-
tion chamber model TE-104 TS RI. The signal counts were electronically
divided by the electron current to compensate for the change in radiation
intensity as a function of electron current as shown in Figure 14.
Therefore, the response of the detection system is linear in the
desired region and comparison of line intensities gives relative cross
sections.

18
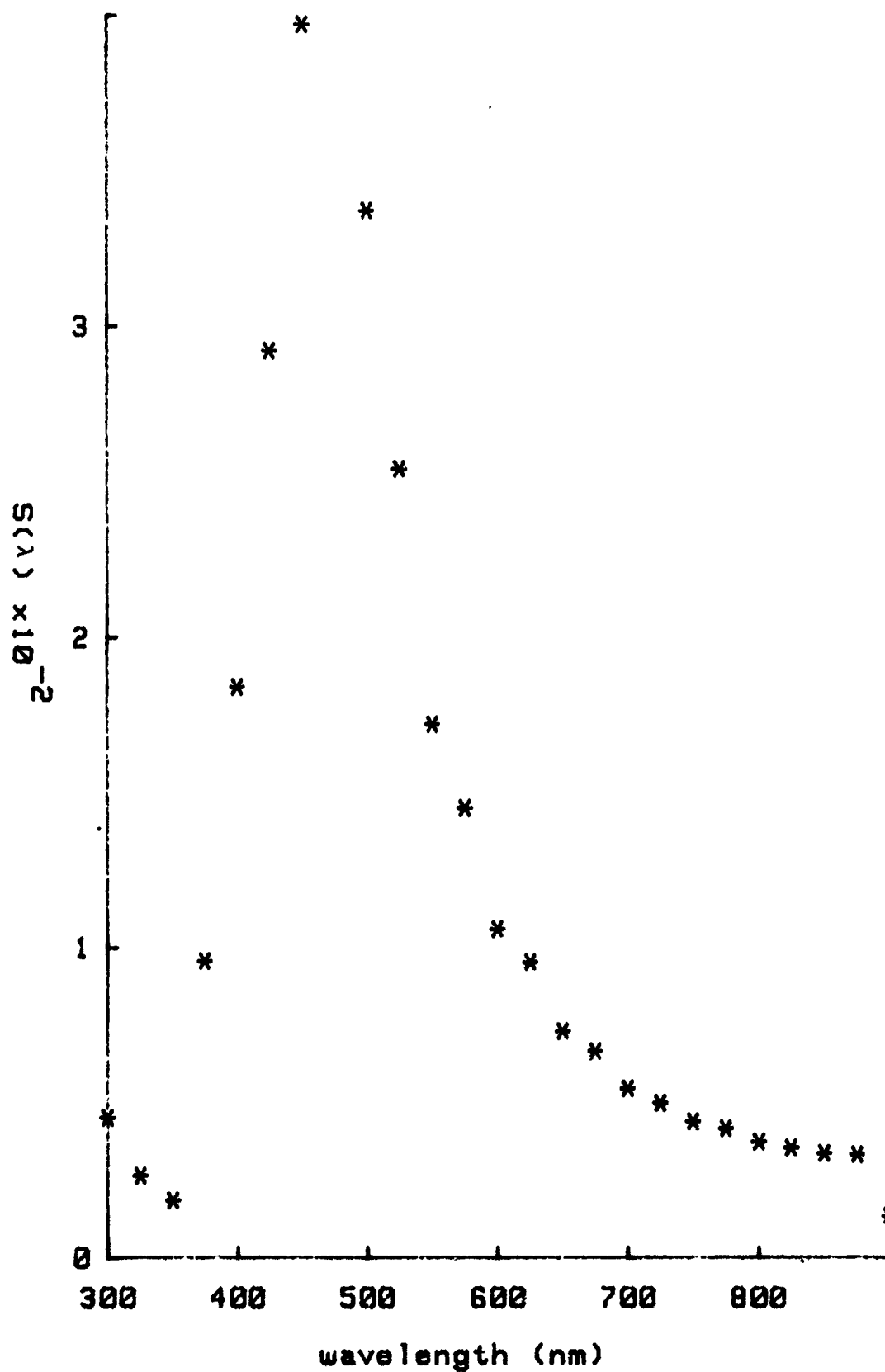
Figure 11. Spectral Sensitivity of Detection System.

19

A block diagram of the apparatus is shown in Figure 12. A signal generator modulates the electron beam to enable discrimination of the light output from the background noise. The light from the observational volume was collected by a lens and focused into the monochromator. Light coming through the monochromator fell on a PMT. The signal was then fed into a narrow-band amplifier and interpreted by a phase-sensitive detector. This information was divided by the electron current and fed into the Y input of an X-Y plotter which plotted this signal against electron energy applied to the X input. Refer to Appendix A for operating procedure.
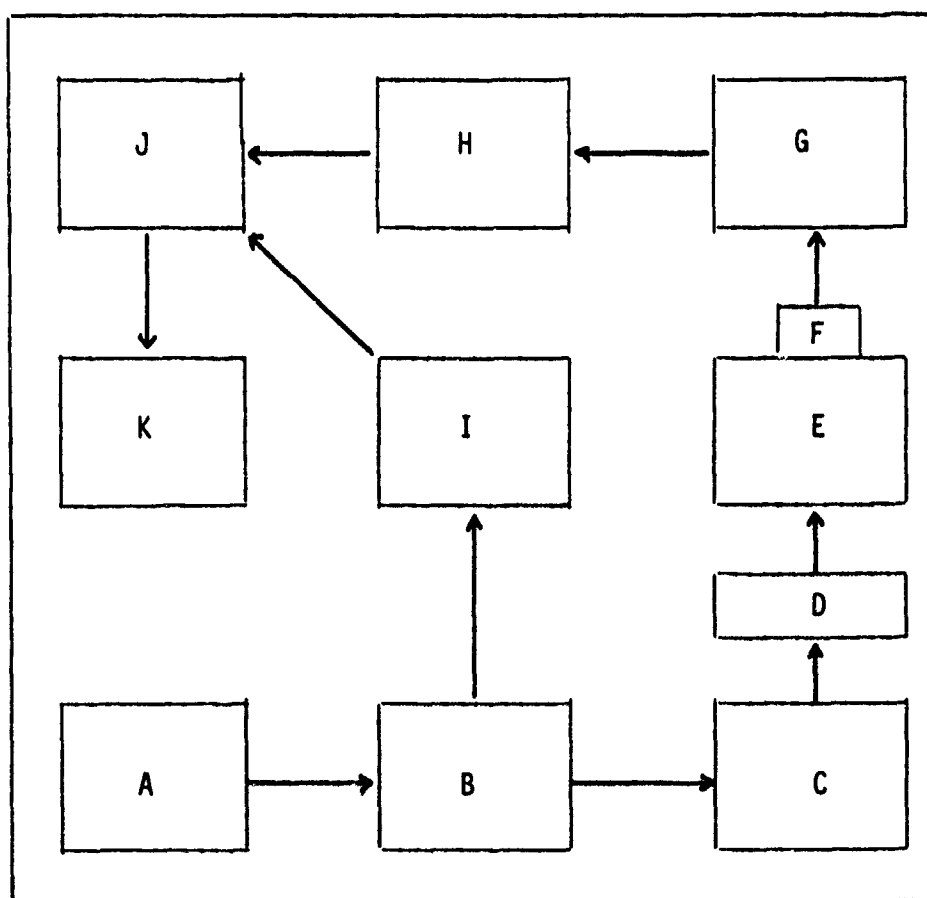
Figure 12. Block Diagram of Apparatus. A, signal generator; B, electron gun; C, interaction volume; D, lens; E, monochromator; F, PMT, G, narrow band amplifier; H, phase sensitive detector; I, current amplifier; J, current divider; K, X-Y recorder.

IV. EXPERIMENT

Linearity Checks

A certain amount of energy smearing occurs in the energy of the electron beam. It is desirable to have a minimum amount of energy spread to ensure adequate determination of electron energy. To check the electron beam energy profile, a series of slits was placed at different heights along the monochromator slit. The intensity was examined at different locations along the diameter of the electron beam. This was done to ensure that the energy spread of the electron beam energy was below 5% from the peak energy (See Figure 13).

It is desirable to have the output signal generated from electron-atom collisions where the electron energy is known. Therefore, it is necessary to ensure that the electrons suffer no other collisions. Thus, it is assumed that if less than one percent of the electrons in the beam suffer inelastic collisions, then the amount of current lost would be negligible:

$$I_c = N\Delta x Q I \quad , \tag{18}$$

where I_c is the collisional current, N is the number density, Δx is the width of the observational volume, Q is the total cross section, and I is the total current. For the criterion above:

$$\frac{I_c}{I} \leq 0.01 \tag{19}$$

Substituting Equation (18) into Equation (19) yields,

$$N\Delta x Q \leq 0.01 \quad . \tag{20}$$
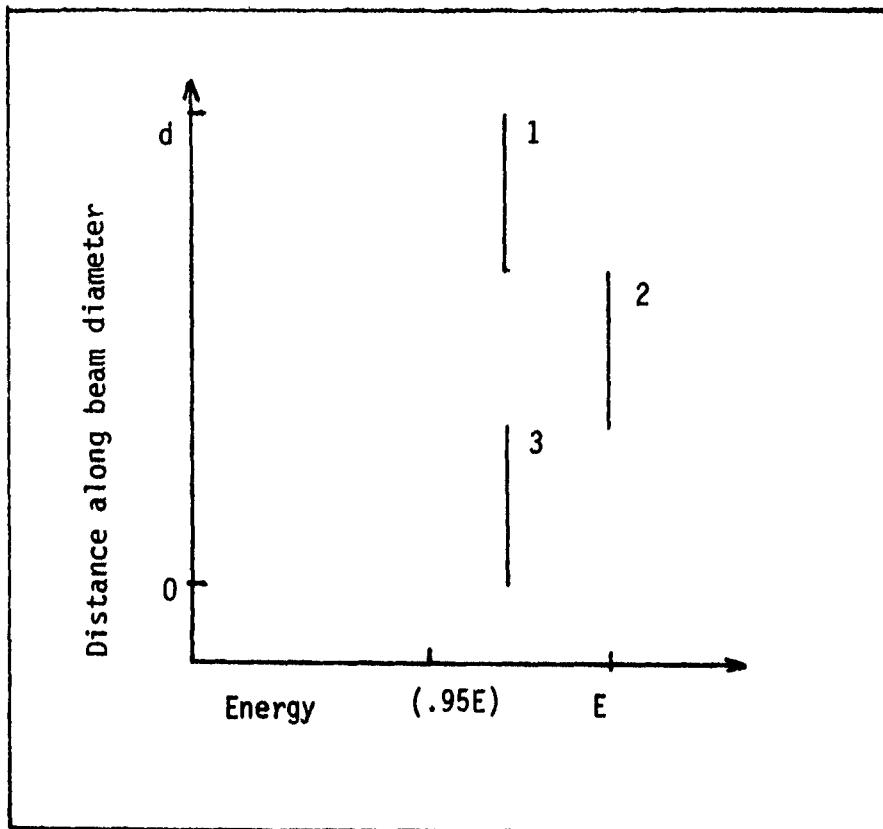
Figure 13. Electron Beam Energy. Measured at various distances along beam diameter.

With a known observational width and an approximate cross section the approximate number density can be obtained (Ref. 1:12). For the system described, the observational width is 1/16 inch and the cross section is approximately 10^{-15} cm^2. Plugging these numbers into Equation (20) and solving for the number density yields:

$$N \approx 4.064 \times 10^{14} \quad \frac{atoms}{cm^3} \quad . \tag{21}$$

Signal vs. Pressure

Certain tests must be performed to demonstrate linearity of the detection system. The first test is to measure signal versus pressure holding electron current, accelerating voltage, and all other parameters
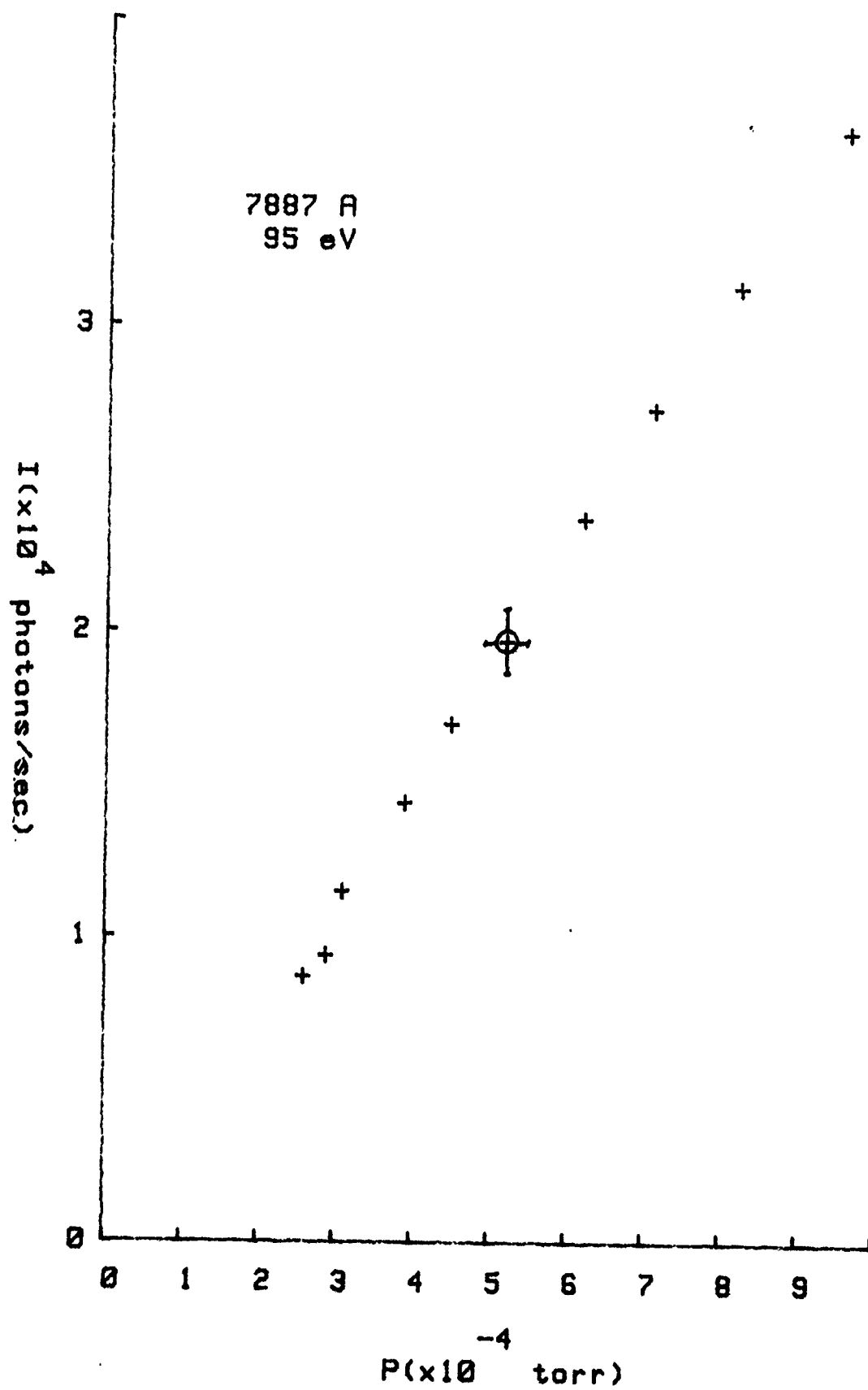
Figure 14. Signal vs. Pressure.

23

constant. The accelerating voltage should be placed far away from the excitation peak to avoid radical signal changes for small shifts in electron energy. A linear response in signal vs. pressure implies that the signal arises from electron-atom collisions, in accord with Equation (1). As the pressure is increased and more atoms are available in the target chamber, then the signal should increase. This test proved to be linear from 2.4×10^{-4} torr to 9.6×10^{-4} torr which is in the working limits of this experiment. The results from this test are displayed in Figure 14. The linearity of this test ensures that the gas density does not increase enough so that a single electron will make multiple collisions and that atom-atom collisions will not occur with consequent energy exchange. If a single electron were to make multiple collisions then the graph would not increase linearly with pressure. The line would rise exponentially as pressure increased if atom-atom collisions cause energy transfer. Since linearity is evident in the graph, changes in pressure will affect intensities of excitation functions only by a linear factor. The cross sections, however, will not be affected because of the number density term in the formulas, providing that the pressure was known and remained constant during individual runs.

Signal vs. Current

The signal was also measured as a function of electron current to test for linearity. The electron current was changed by varying the drawout potential of the electron gun. Pressure, accelerating voltage and all other parameters were held constant. The accelerating voltage was set at a high voltage (95 V) for the same reason as in the signal versus pressure test, namely to avoid radical signal changes for small shifts in electron energy. The signal versus current test ensures that

24

no appreciable multiple excitations occur in the observation region. The results are given in Figure 15. The linearity of this graph shows that the collected radiation intensity was directly proportional to the electron current. Therefore, the signal was divided automatically by the current to compensate for changes in the electron current. The deviation from linearity at currents greater than 250 μamps results from energy loss due to electron-electron collisions. Only currents in the linear portion of this graph were used to collect data.

Comparison to Previous Measurements

Excitation functions for helium transitions have been measured by previous researchers and are well known. Therefore, remeasurement of some of these excitation functions provide a suitable test for the accuracy of the apparatus. The initial attempt proved futile because the signal-to-noise ratio was low and the shape of the excitation function was indeterminable. Since the signal was visible with the naked eye and the dark room provided no appreciable noise level, it was deduced that the entire signal was not being collected. Alignment of the optical detection system decreased the noise level and concurrently increased the signal strength. When the excitation function of the He 3889 $\overset{o}{A}$ transition was then obtained, it was found to have a shape disagreement with previously published data. Figure 16 shows a comparison of the result from the initial measurement of this work to the shape measured by I. P. Sapesochnyi and P. V. Felstan (Ref. 11). The rise in the excitation function at high energy was suspected to result from focusing of the electron beam as a function of accelerating voltage, coupled with inadequate optical collection of the observation volume.

25
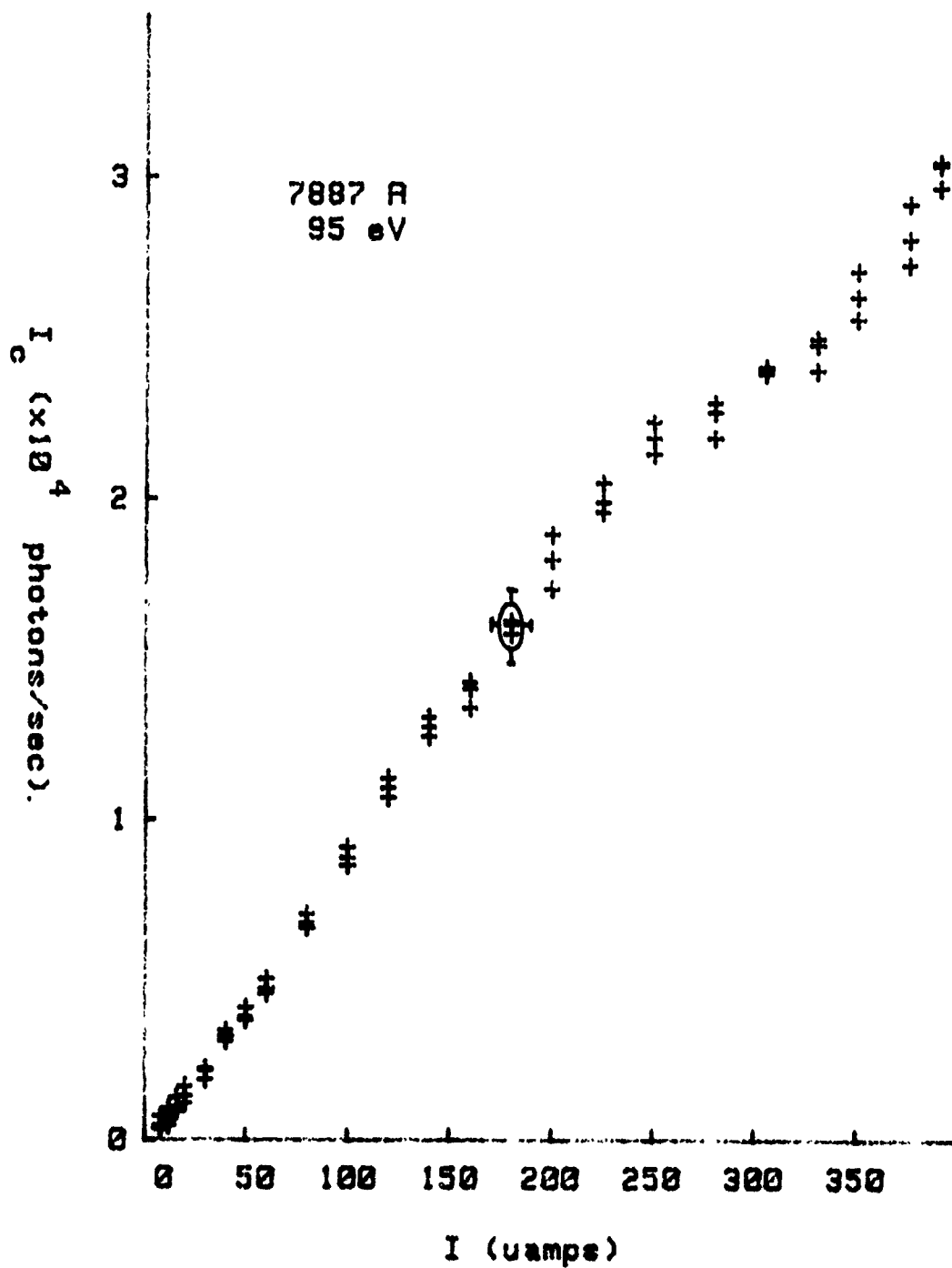
Figure 15. Signal vs. Current.

Referring to Figure 3, this means that the area of observation $h\Delta x$ is larger than the area of the monochromator slit. Equation 3 dictates that the entire area through which electrons pass must be collected by the optics in order to accurately describe the physical interaction which is the subject of research. The detection system up to this point was aligned so that there was unit magnification of the image of the electron beam on the slits of the monochromator. In order to correct for inadequate collection of the image, the system was realigned using magnification of one half. Therefore, the monochromator slit height of 1 cm is approximately a factor of two larger than the image of the 1 cm diameter electron beam. The excitation function for the 3889 $\overset{o}{A}$ transition measured subsequent to the magnification reduction is displayed in Figure 17. The results of I. P. Zapesochnyi, J. H. Lees (Ref. 12), F. L. Miller (Ref. 13), and H. R. M. Moussa (Ref. 14), shown in Figure 18, were used as a basis for determining the accuracy of the apparatus. The data obtained in this work is comparable to I. P. Zapesochnyi's result.

FIGURE 16. Comparison of Shapes from Early Measurements.

Figure 17.   Excitation Function for Helium 3889 Å Transition.

Figure 18.   Results of Previous Measurements (Ref. 15:11).
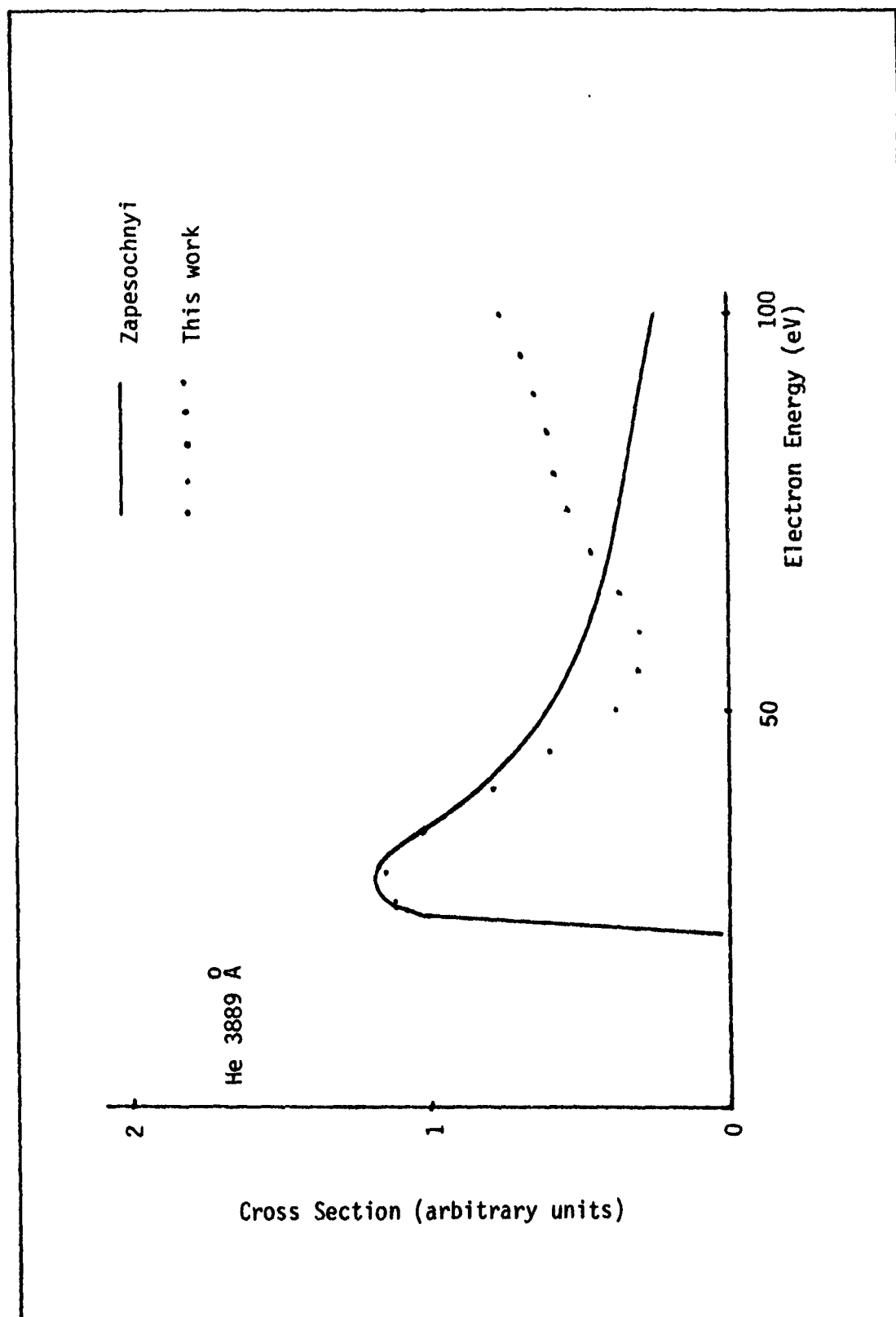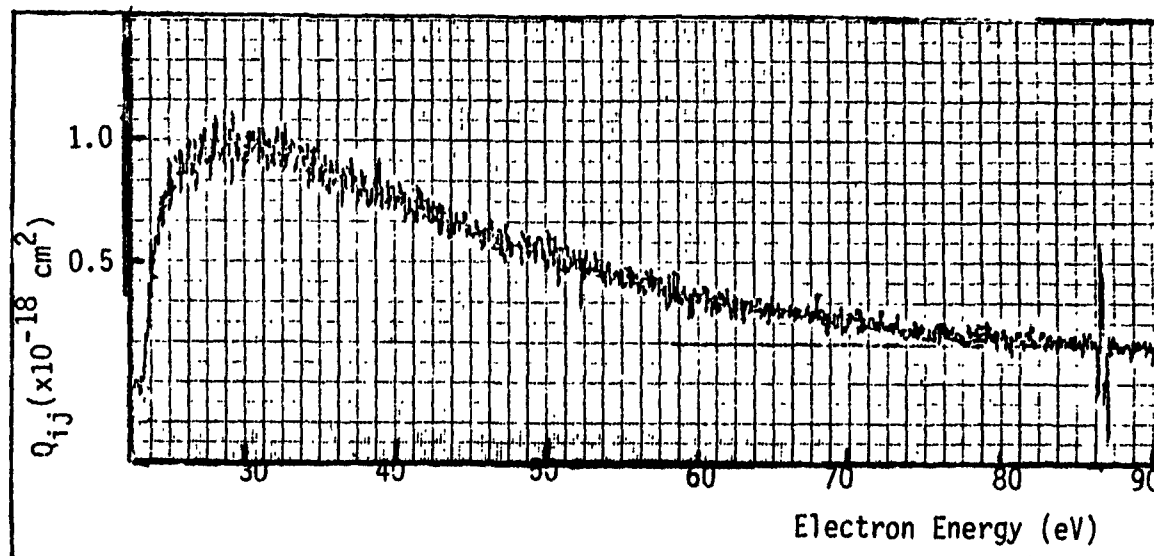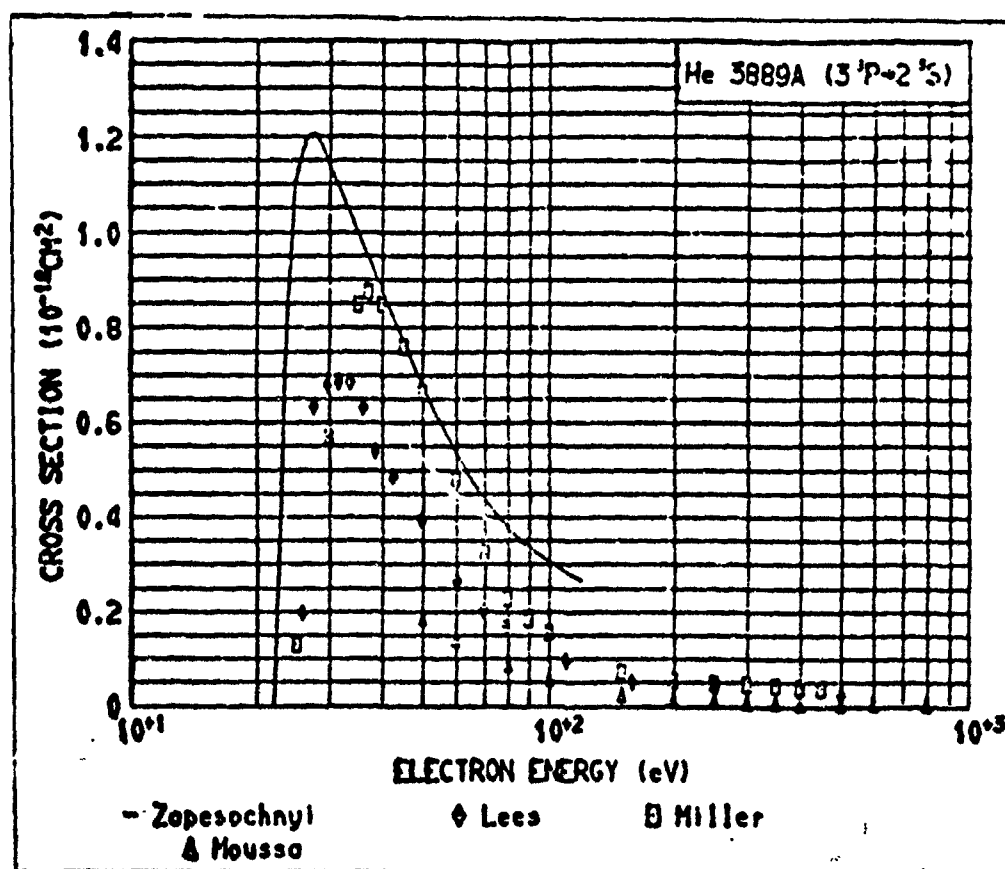
V. STANDARDIZATION

Transmission Factors

The detection system must be standardized to make absolute measurements. The standardization procedure consists of determining the spectral sensitivity of the detectors by use of a calibrated tungsten ribbon lamp. The solid angle of radiation which is gathered by the lens is given by:

$$\Omega = \frac{\pi R^2}{S_0} \tag{22}$$

where R is the radius of the lens and S_0 is the object distance. A magnification of $\frac{1}{2}$ was obtained by setting S_0 equal to twice the length of S_1 (see Figure 19). This ensures that the entire image will fall on the monochromator slit. The lens radius is 3.0 cm, the object distance is 40.0 cm, and therefore the solid angle is 1.77×10^{-2} str. The slit width, w, of the monochromator will be the length of the observation region, Δx. The radiation must pass through the chamber window and the lens. These optical elements have transmission factors given by t_w and t_L respectively. The transmission factor for the monochromator is given as (Ref. 16:25),

$$t_M = \begin{cases} 1 + \dfrac{\lambda - \lambda_0}{\Delta \lambda} & \text{for } \lambda_0 - \Delta \lambda \leq \lambda \leq \lambda \\[2ex] 1 - \dfrac{\lambda - \lambda_0}{\Delta \lambda} & \text{for } \lambda_0 \leq \lambda \leq \lambda_0 + \Delta \lambda \end{cases} \tag{23}$$

where $\Delta \lambda$ is the monochromator bandpass and λ_0 is the peak of the transmission function. These values are further illustrated in Figure 20.

The entrance and exit slits must be equal in order for the above conditions, including Equations (22) and (23), to hold. The Jarrel-Ash
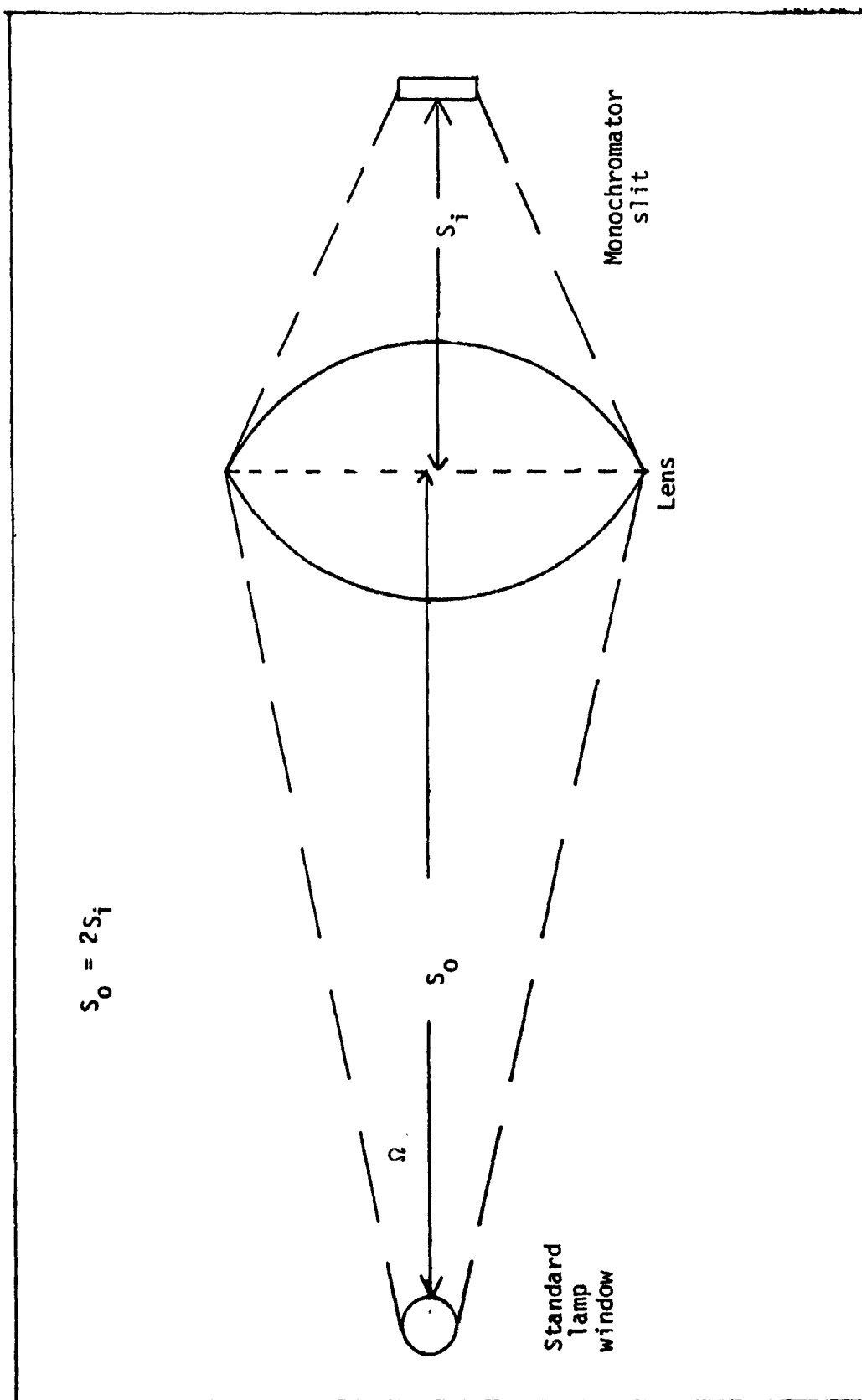
Figure 19. Optical Pathlengths.
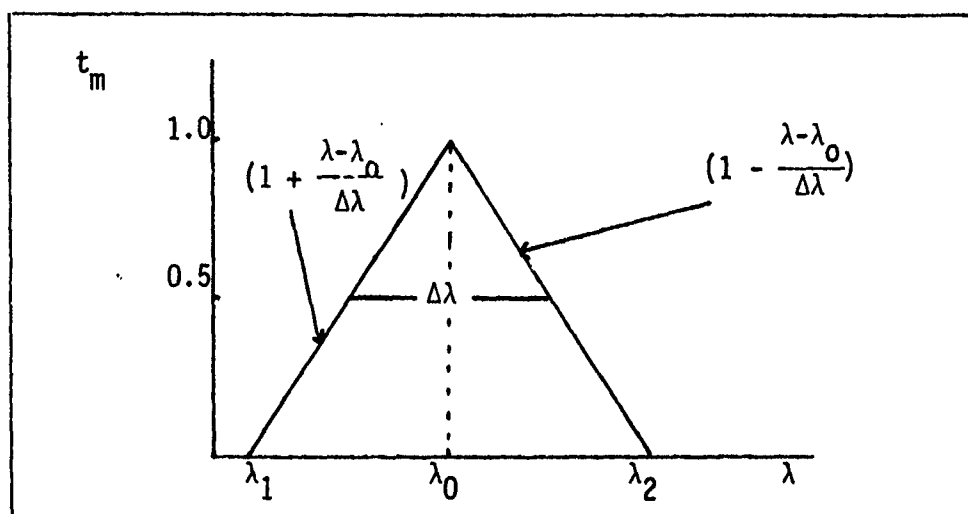
Figure 20. Monochromator Transmission Factor versus Wavelength.

half meter monochromator has a bandpass of 8 $\overset{\text{o}}{\text{A}}$ at 6000 $\overset{\text{o}}{\text{A}}$ for slit widths of 400 microns.

For simplification in standardization procedures, a standard lamp source was measured at a wavelength of 6000 $\overset{\text{o}}{\text{A}}$. In this case, the transmission factor of the monochromator is unity, which results in maximum intensity. The cross section can then be written using Equations (15) and (22):

$$Q_{ij} = \frac{4\, S_o^2\, I_c e}{R^2 \Delta x N I t_W t_L S(\lambda)} \quad . \tag{24}$$

Calibration

In order to calculate the spectral sensitivity, a General Electric standard lamp type GE 30A/T24/7 was used in the standardization procedure. It has a tungsten ribbon filament located approximately 10 cm. behind a fused silica output window. The output window is three centimeters in diameter.

The spectral radiant flux, P_λ, of the standard lamp is given by,

32

$$P_\lambda = R_\lambda N_\lambda sA/D^2 \quad ; \qquad\qquad (25)$$

where,

R_λ = spectral reflectance of combination of mirrors (0.84)

N_λ = spectral radiance of standard (50.00 μW/str-m -mm^2 at 6000 $\overset{o}{A}$)

s = area of spectrometer slit (2.25 mm^2)

A = area of limiting optic (706.9 mm^2)

D = distance of optic from slit (400 mm).

Therefore the spectral radiant flux of the standard lamp at 6000 $\overset{o}{A}$ is 64.8 μW/mu.

To ensure that the solid angles and optical path lengths of the standard lamp and collision chamber are essentially equal, it was decided that the monochromator, detector, and imaging lens be placed on a movable table. The table could be moved in a direction perpendicular to the optical paths of radiation. The standard lamp was mounted beside the collision chamber so that the optical paths were parallel. The standardization arrangement is shown in Figure 21.

The output of the photomultiplier tube (PMT) in the standardization configuration is given by Walker (Ref. 4:28) as:

$$I_S = S(\lambda)A_S \Omega_S t_S t_L \int_{\lambda_0 - \Delta\lambda}^{\lambda_0 + \Delta\lambda} R_N(\lambda, T)t_m d\lambda \quad , \qquad (26)$$

where,

A_S = area of tungsten ribbon from which photons are collected by the monochromator

Ω_S = solid angle from which light is collected in the standardization arrangement

33

Figure 21. Standarization Configuration.
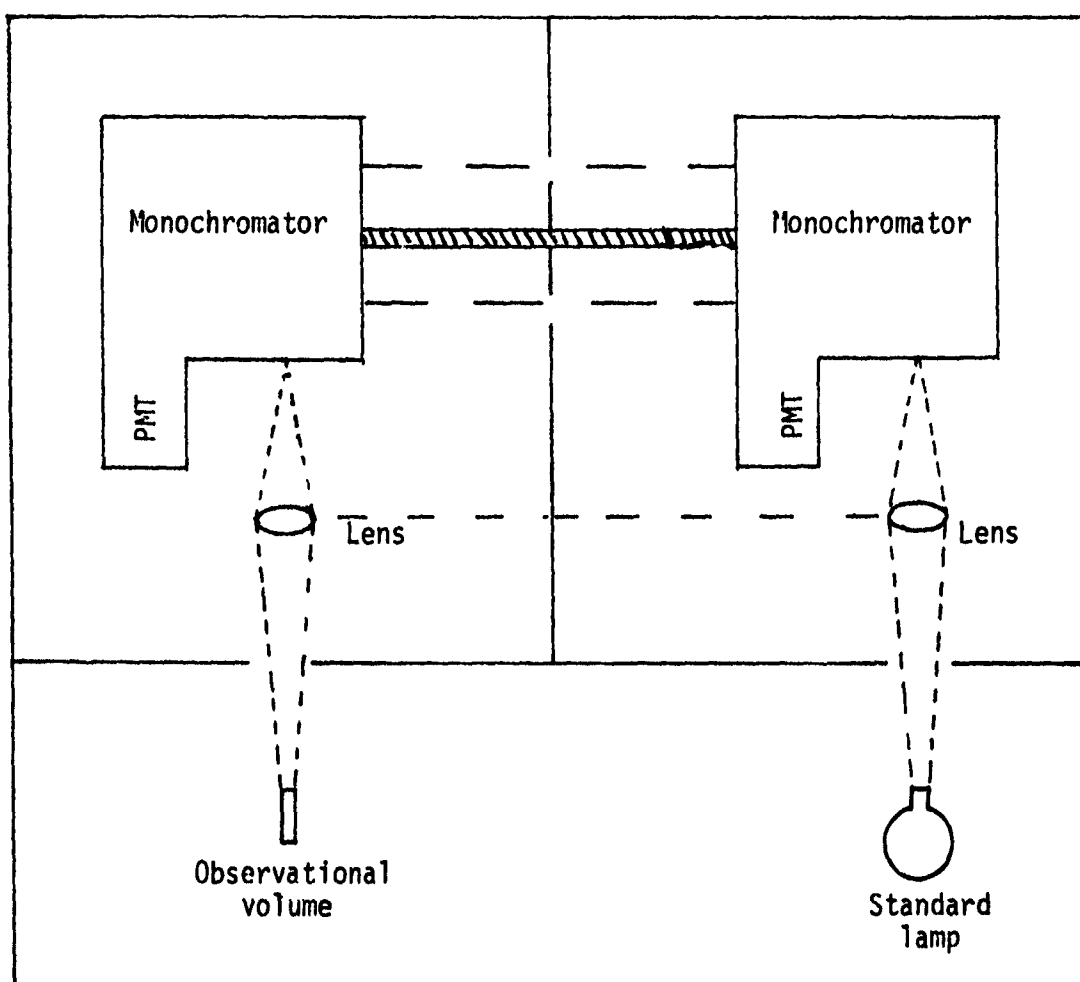
t_S = transmission factor of the standard lamp window

$R_N(\lambda, T)$ = photon radiancy.

The photon flux hitting the detector, F_S, can be defined as,

$$F_S = A_S \Omega_S t_S t_L \int_{\lambda_0 - \Delta\lambda}^{\lambda_0 + \Delta\lambda} R_N(\lambda, T) t_m d\lambda \quad ; \qquad (27)$$

which simplifies Equation (26) to,

$$I_S = S(\lambda) F_S \qquad (28)$$

34

The photon radiancy gives the rate of photon emission per unit wave-length interval into unit solid angle normal to the surface whose temperature is T. The tungsten can be approximated as a graybody(Ref. 4:29) because,

$$R_N(\lambda,T) = e(\lambda,T)R_N^B (\lambda,T) \quad , \tag{29}$$

where $e(\lambda,T)$ is the emissivity of the tungsten ribbon and $R_N^B (\lambda,T)$ is the blackbody photon radiancy.

St. John (Ref. 17:30) shows that division of power radiancy, I_N^B, by hc/λ gives photon radiancy:

$$R_N^B (\lambda,T) = I_N^B (\lambda,T) \frac{\lambda}{hc} \quad . \tag{30}$$

The power radiancy is given by the expression,

$$I_N^B = \frac{2hc^2}{\lambda^5} \frac{1}{(e^{hc/\lambda KT}-1)} \quad , \tag{31}$$

which means,

$$R_N^B (\lambda,T) = \frac{c_1}{\pi hc\lambda^4} \frac{1}{(e^{c_2/\lambda T}-1)} \tag{32}$$

where

$$c_1 = 3.7405 \times 10^{-16} \text{ W-m}^2$$
$$c_2 = 1.43879 \times 10^{-2} \text{ m-}^o\text{K} \quad .$$

The integral in Equation (26) for a $\Delta\lambda$ of 16 $\overset{o}{A}$,

$$R_{16}(\lambda_o,T) \quad \int_{\lambda_o-16\overset{o}{A}}^{\lambda_o+16\overset{o}{A}} R_N^B(\lambda,T) e (\lambda,T)t_m d\lambda \quad , \tag{33}$$

has been calculated by J. D. Jobe (Ref. 18:14) to be approximately

35

$$R_{16}(\lambda_o,T) = \frac{16\overset{o}{A}}{\Delta\lambda} e(\lambda,T) R^B_{\Delta\lambda}(\lambda_o,T) \quad . \tag{34}$$

The emissivity $e(\lambda,T)$ is a slowly varying function of wavelength and was, therefore, assumed to be constant. Equation (34) is good within one percent for values of $\Delta\lambda < 100\overset{o}{A}$ if $T < 3000^o$ K and $\lambda_o > 2200 \overset{o}{A}$. Only the linear terms in the Taylor expansion for $R^B_N(\lambda,T)$ about λ_o were integrated over. Using Equations (27) and (28) with Equation (34) produces

$$S(\lambda) = \frac{16\overset{o}{A} I_S}{A_S \Omega_S t_S t_L \Delta\lambda \, e(\lambda,T) R^B_{16}(\lambda,T)} \quad . \tag{35}$$

Combining this with Equation (22) yields,

$$Q_{ij} = \frac{4S_o^2 I_c e\Delta\lambda \, e(\lambda,T) R^B_{16}(\lambda,T) t_s}{16\overset{o}{A} I_S I N t_w R^2 \Delta x} \quad . \tag{36}$$

The chamber window is composed of sapphire and the standard lamp window is fused silica. The transmission factor for both windows is fairly constant over the wavelength region examined. The transmission factor for sapphire is approximately 82% and that of fused silica is 90%. Therefore, the ratio of transmission factors,

$$\frac{t_s}{t_w} = 0.91 \quad , \tag{37}$$

and, therefore,

$$t(\lambda) = 0.74 \quad . \tag{38}$$

VI. CONCLUSION

Technique Improvements

Two critical considerations in electron gun design are the mounting
of the insulating feed through in the faceplate of the copper shield and
the gold plating of the copper shield. The wires which were used to
apply potentials to the electron gun grids were fed through the copper
faceplate in alumina insulators. The insulators were initially mounted
in the copper shield with epoxy. The heat produced during the activa-
tion process caused the epoxy to burn. An oxide was produced and
deposited on the alumina insulators, thus shorting out the electron
gun. Careful investigation resulted in the use of Ceramabond, an
alumina based cement, as a replacement for epoxy.

The gold plating of the copper shield was an attempt to prevent
oxidation of the shield and to deter absorbtion in the infrared
However, the gold was also affected by the heat of activation. As the
shield became hot, the gold diffused into the copper. Examination of
the properties of gold showed that the shield must be cooled when the
heater current is greater than one amp. The temperature increase due
to the filament is sufficient to cause gold to diffuse into copper and
to burn epoxy.

The copper shield completely surrounded the electron gun and,
thus, radiation was scattered from the inside walls of the shield. This
radiation reflected through the observation slit. In attempts to align the
monochromator, reflected radiation created a large background signal.
An attempt was made to minimize the noise by cutting a 1/16 inch slit
opposite the observation slit. Nevertheless, significant reflection

37

occurred, so the gun was removed and the opposite slit was enlarged
to 3/16 inch. The reflected radiation was reduced, but a small amount
was still detectable.

Results

All results were taken in the regions where the output radiation
was proportional to the pressure and the electron gun current. The
appearance potential in all cases was found to be within 2 eV of the
spectroscopic value published in Striganov and Sventitski (Ref. 19:571).
However, the relative intensities shown in the tables do not compare
with those shown here. There is a difference between relative inten-
sities of various lines excited by a discharge and those excited by a
monoenergetic electron beam (Ref. 20:4). Therefore, tabulated intensity
ratios are insufficient for interpretation of the xenon spectrum.
Generally, excitation functions for xenon I lines have maximum cross
sections at energies between 16 eV and 22 eV. An example is shown in
Figure 22. This figure shows the actual data obtained by the experi-
mental configuration shown in Figure 12. These lines have sharp peaks
at the maximum and slope downward at higher electron energies, Figure
23 shows an excitation function with a maximum at an electron energy
between 16 eV and 22 eV, but the cross section remains approximately
constant at higher energies. The characteristic shape of the excitation
function has been extracted in order to eliminate possible confusion
resulting from scale changes and minute line divisions on the raw data.
Some excitation functions have a slight "hump" around 30 to 70 eV. This
"hump" in most cases is probably caused by cascading from higher states.
As the electron energy is increased, the bombarding electrons may excite

38
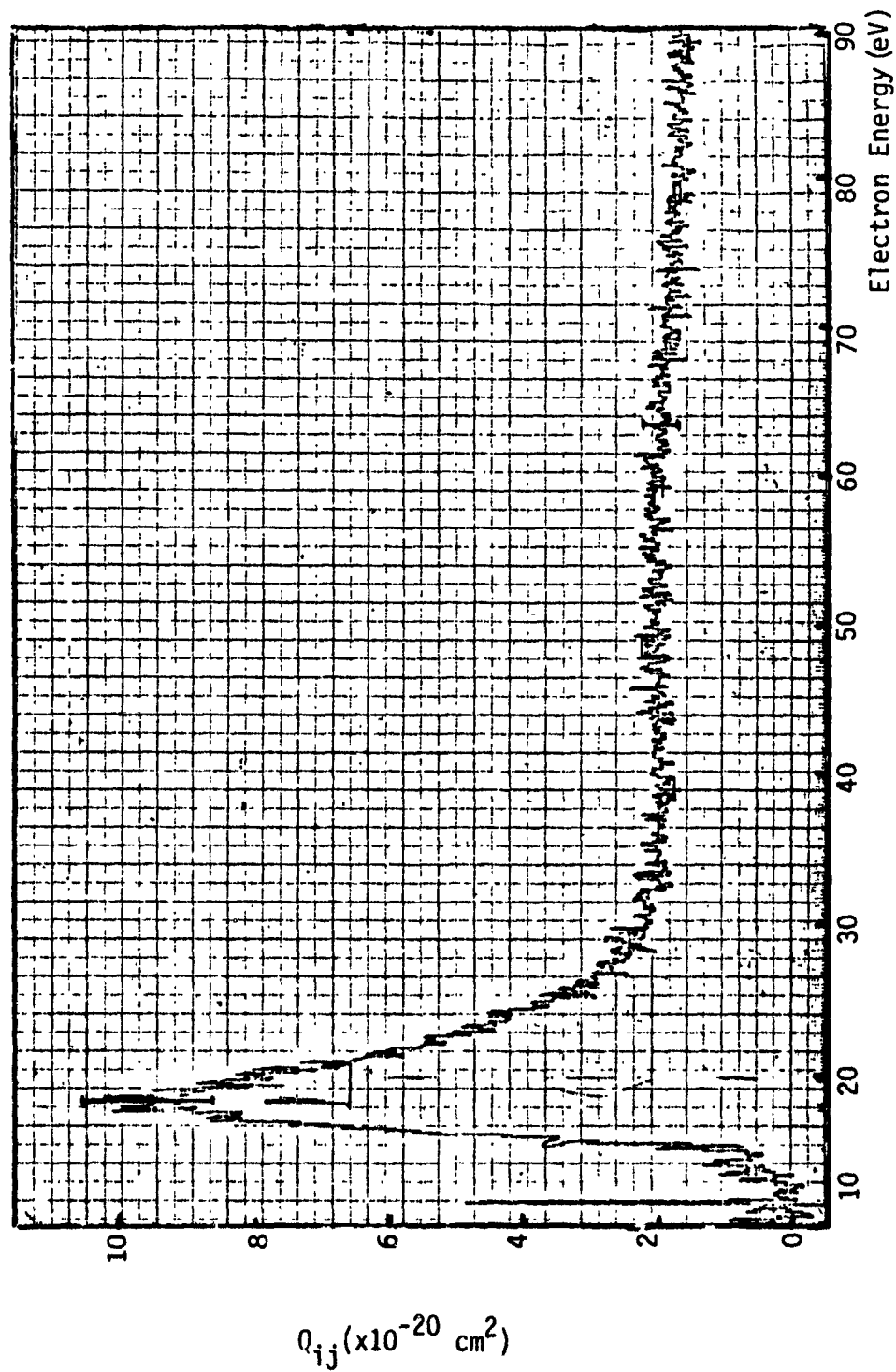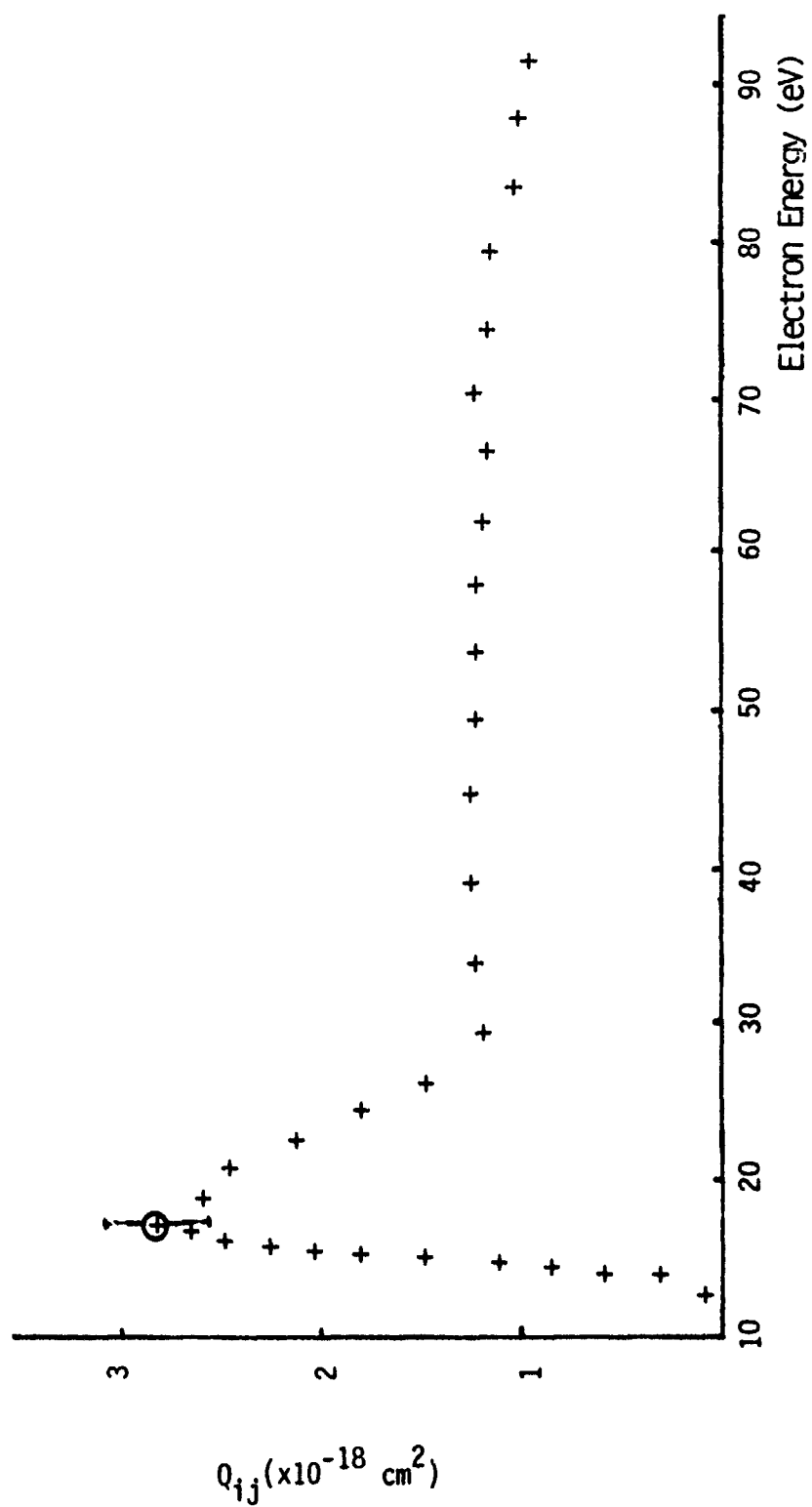
Figure 22. Xe 4697 Å $(7p[\tfrac{1}{2}] \rightarrow 6s [1\tfrac{1}{2}]°)$

$Q_{ij} (\times 10^{-20} \ cm^2)$

39

Figure 23. Xe 7336 Å $(5d'[2\tfrac{1}{2}]° \rightarrow 6p[2\tfrac{1}{2}]°)$

Q$_{ij}$(x10^{-18} cm^2)

Electron Energy (eV)

40

levels at higher energies than the level we are observing. These atoms in higher excited levels make a series of energy level transitions to eventually reach the ground state. Thus, the energy level we are observing may be populated following decay from atoms excited to higher states, as well as from direct excitation of ground state atoms. This former process is called cascading and an example of this can be seen especially well as a hump from 40 - 90 eV on the excitation function for the 6318 $\overset{o}{A}$ transition shown in Figure 24. The apparent drop in cross section at 15 eV was due to a change in scale which was not manually adjusted at the proper time.

Figure 23 (5d'$[2\frac{1}{2}]°{\rightarrow}6p[2\frac{1}{2}]°$) and Figure 24 (8d$[3\frac{1}{2}]°{\rightarrow}6p[2\frac{1}{2}]°$) show excitation functions for transitions from d levels and both exhibit sharp peaks. These figures also show that d level transitions have large cascade contributions.

Generally broader excitation functions have maximum cross sections at electron energies greater than 25 eV. The s level transitions appear to have broadly peaked excitation functions as displayed by Figure 25 (8s$[1\frac{1}{2}]°{\rightarrow}6p[2\frac{1}{2}]°$). This excitation function for the 7803 $\overset{o}{A}$ transition has a step or plateau at electron energies near 20 eV. The contribution due to cascading overlaps the direct excitation contribution. Therefore, the initial rise is due to the direct contribution to the level being examined and the "hump" results from cascading effects. Figure 26 shows the excitation function for the 8576 $\overset{o}{A}$ transition which has two maxima: a sharp peak at 15 eV and a broader peak at 27 eV. The excitation function for the 4807 $\overset{o}{A}$ transition shown in Figure 27 also has a double peak, but the peaks are spaced only 1.5 eV apart. These double peaks are also believed to be a result of cascading.

Figure 24. Xe 6318 $\overset{\circ}{A}$ $(8d[3\tfrac{1}{2}]° \rightarrow 6p[2\tfrac{1}{2}]°)$

Electron Energy (eV)

$\sigma_{ij}(\times10^{-19}\text{cm}^2)$
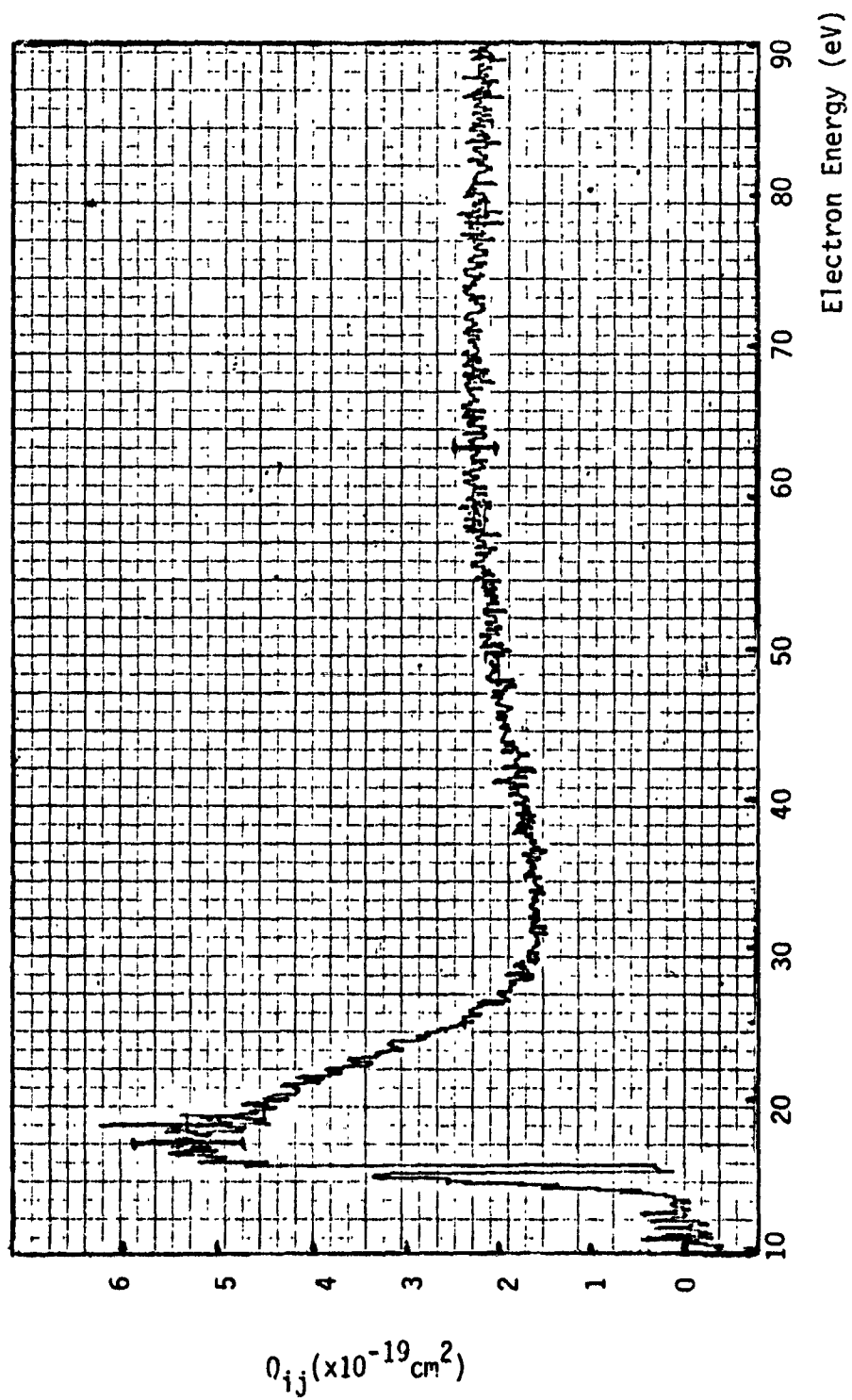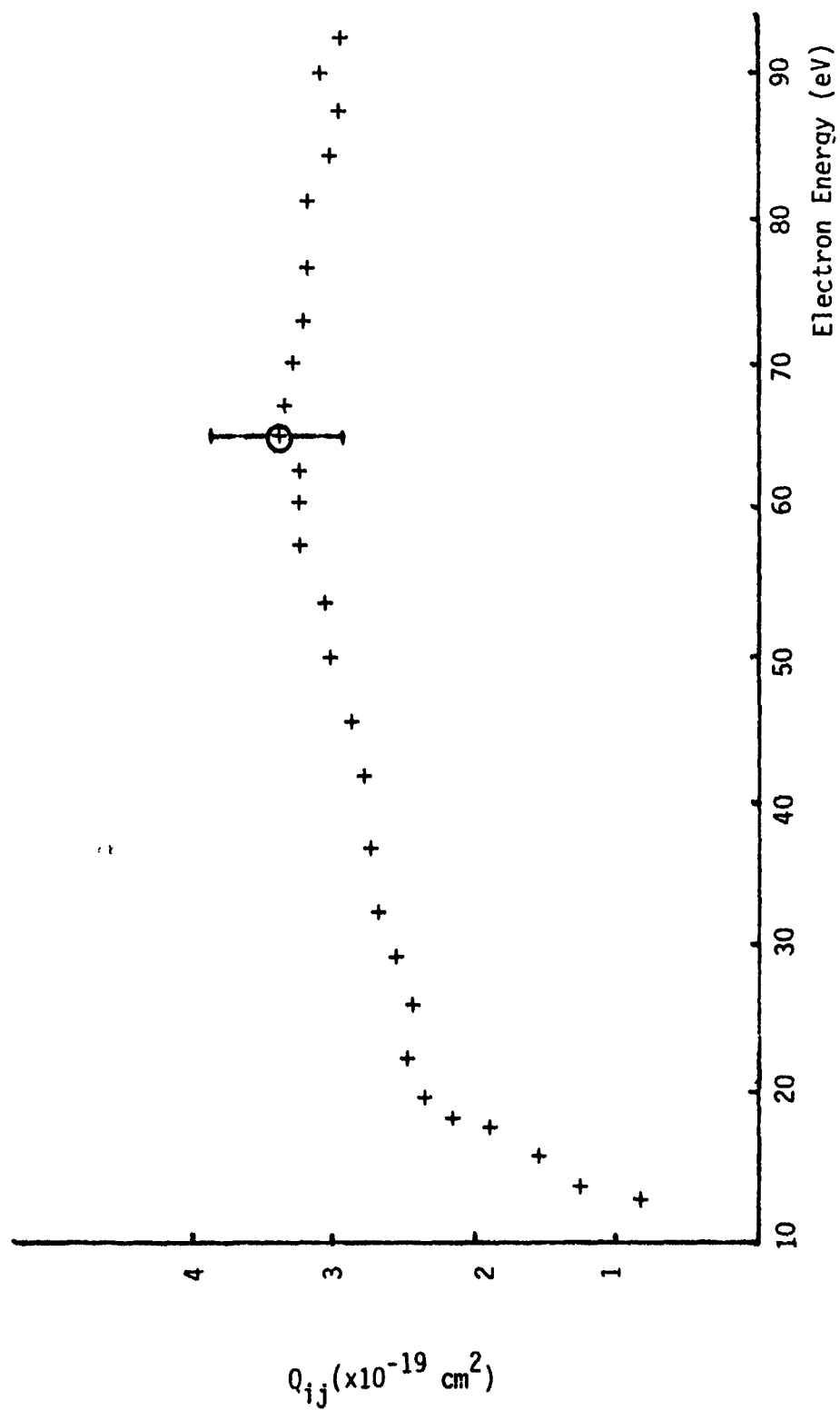
Figure 25. Xe 7803 Å $(8s[1\tfrac{1}{2}]^\circ \rightarrow 6p[2\tfrac{1}{2}]^\circ)$

43
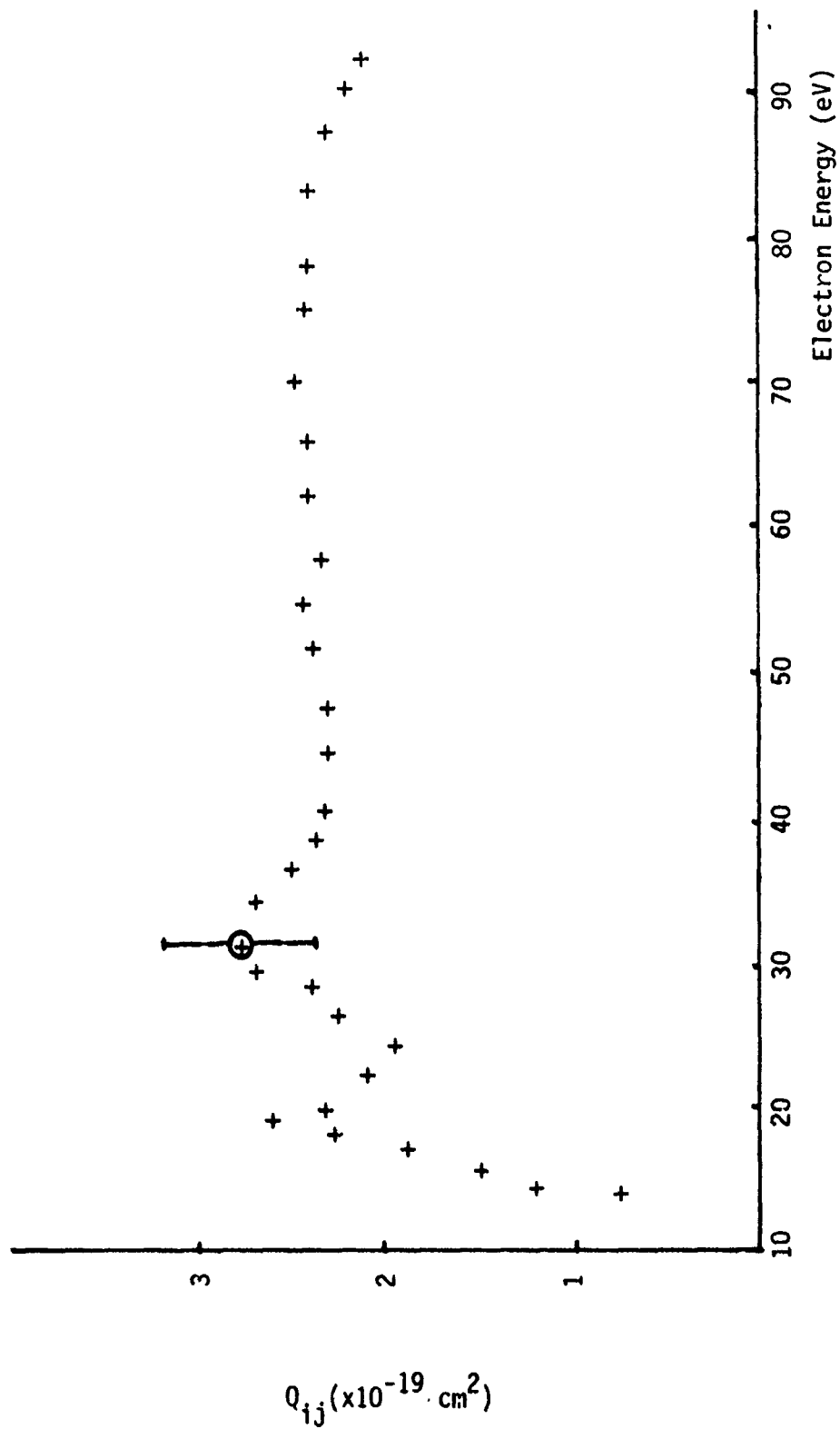
Figure 26.   Xe 8576 Å (7p[½]→6s'[½]°)

44

Figure 27.   Xe 4807 Å $(7p[\frac{1}{2}] \rightarrow 6s[1\frac{1}{2}]°)$

45

The shapes of all excitation functions depend only upon the characteristics of the ground state and the upper excited state. The shapes can be predicted by use of the Born Approximation and the resulting relation:

$$Q_{01} = 2\pi \int_0^\pi C \left\{ \int \Psi_0 e^{i(k_0-k_1)r_1} \Psi_1^* \, dr \right\} \sin\theta d\theta , \qquad (39)$$
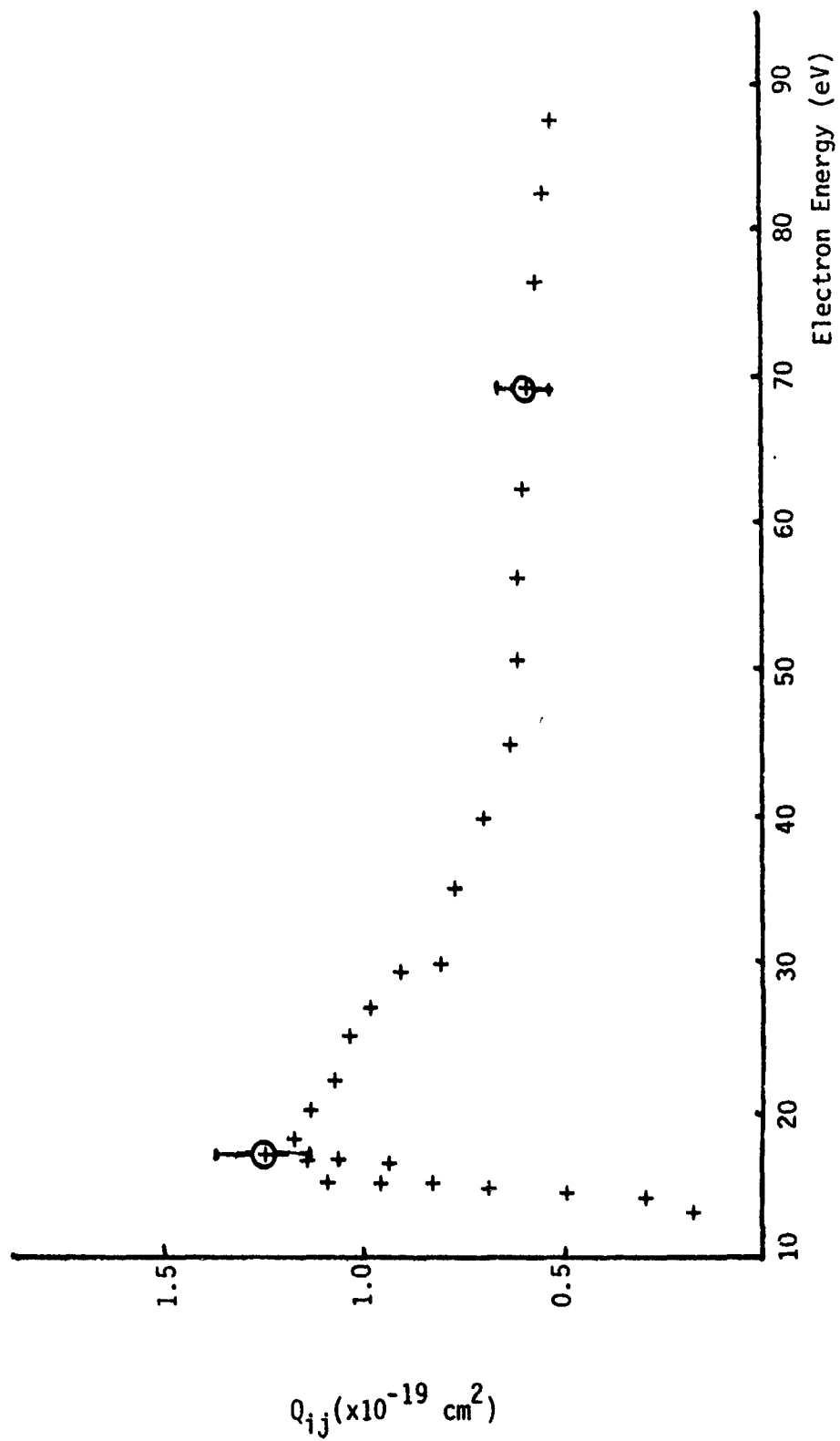
where Ψ_0 is the wavefunction for the ground state, k_0 and k_1 are the wavenumbers for the respective states, r_1 is the separation distance, and Ψ_1 is the wavefunction for the excited state (Ref. 21:436).

The data obtained shows that the d level transitions have sharply peaked excitation functions and the s level transitions appear to have more broadly peaked excitation functions. However, the p level transitions have excitation functions with shapes which seem to vary according to the value of the angular momentum J of the upper level. The excitation functions for upper level J values of one, two, and three are sharply peaked. An excitation function for J=1 is shown in Figure 28. Figures 29-32 display sharply peaked excitation functions for J=2. Examples of excitation functions for upper levels with values of J=3 are presented in Figures 33 and 34. However, excitation functions for transitions from upper excited levels which have zero angular momentum are more broadly peaked. Figures 35 and 36 show examples of the broad excitation functions for p level transitions.

An analysis of the coupling scheme which best describes the xenon excitation cross sections was felt to be beyond the scope of this work. No comparison with helium is made because helium subscribes well to LS coupling, while xenon is better described by jℓ coupling (Ref. 22:537).

46
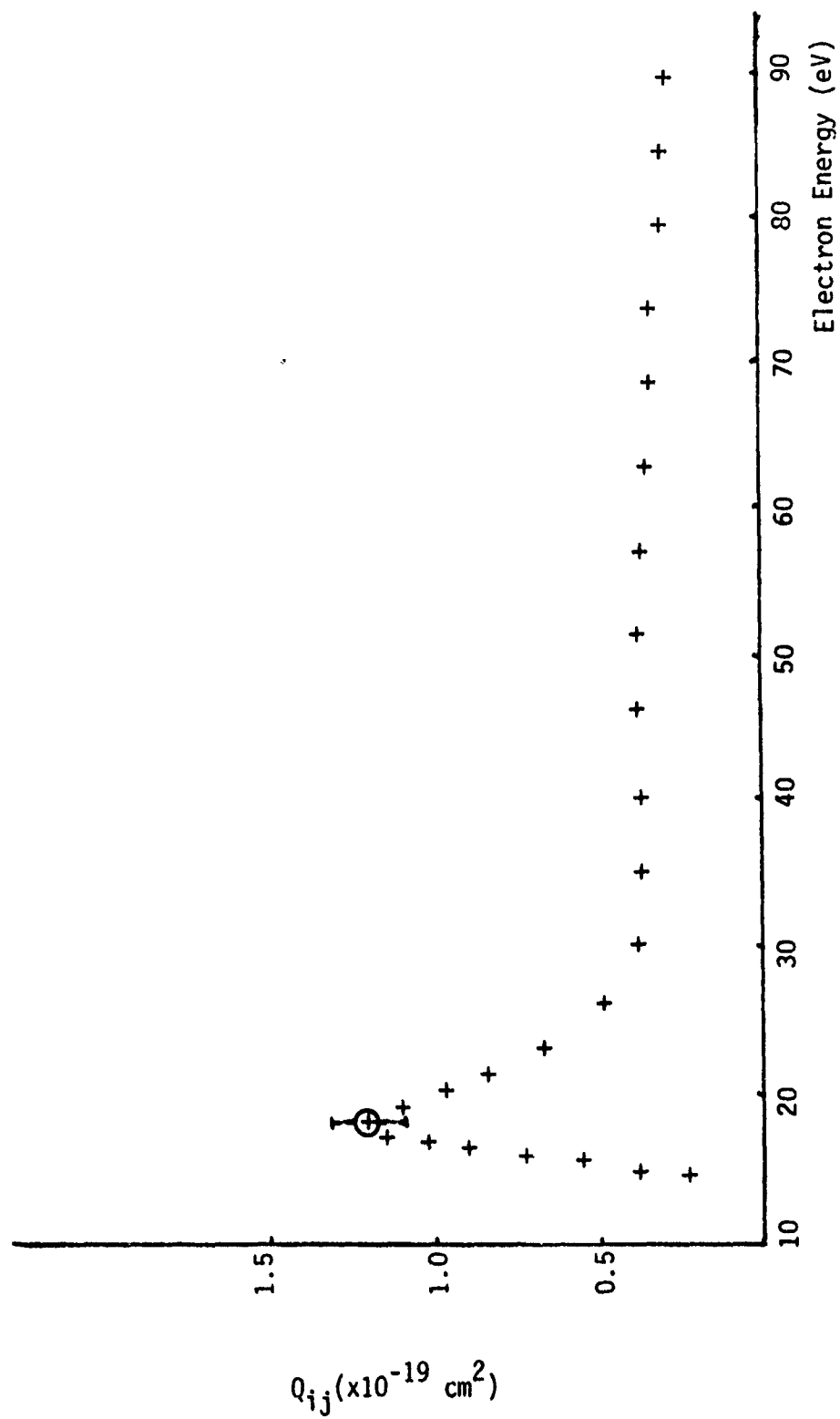
Figure 28. Xe 4830 Å ($7p[2\frac{1}{2}] \rightarrow 6s[1\frac{1}{2}]°$)

47

Figure 29. Xe 4501 Å (6p' [½]→6s [1½]°)

$Q_{ij}(\times 10^{-20} \text{ cm}^2)$

Electron Energy (eV)

48

Figure 30.   Xe 4734 Å (6p' [1½]→6s [1½]°)

Electron Energy (eV)

$Q_{ij} (\times 10^{-20} \ cm^2)$

49

Figure 31. Xe 8231 Å (6p[1½]→6s[1½]°)

$0_{ij}(\times 10^{-18}$ cm$^2)$

Electron Energy (eV)

50
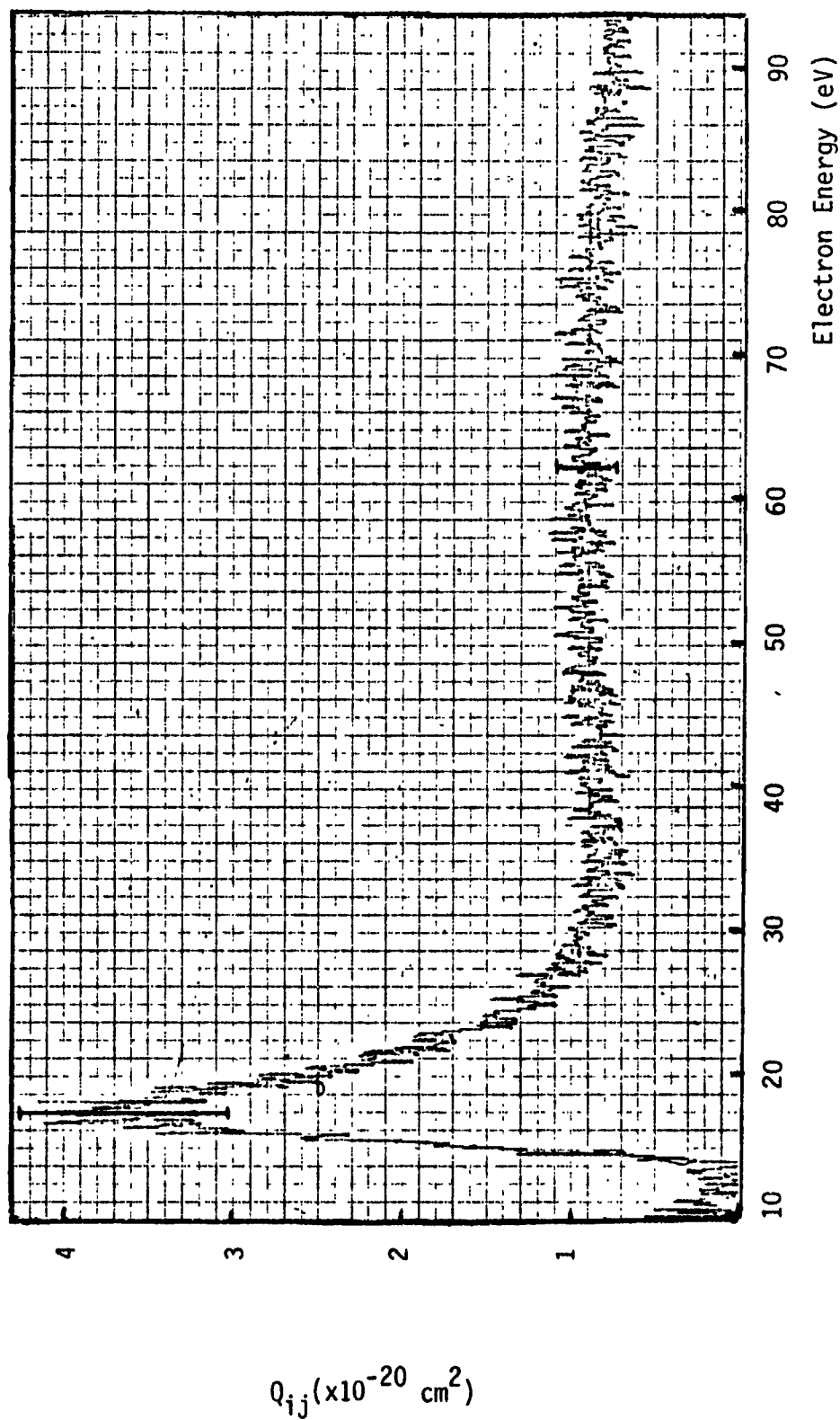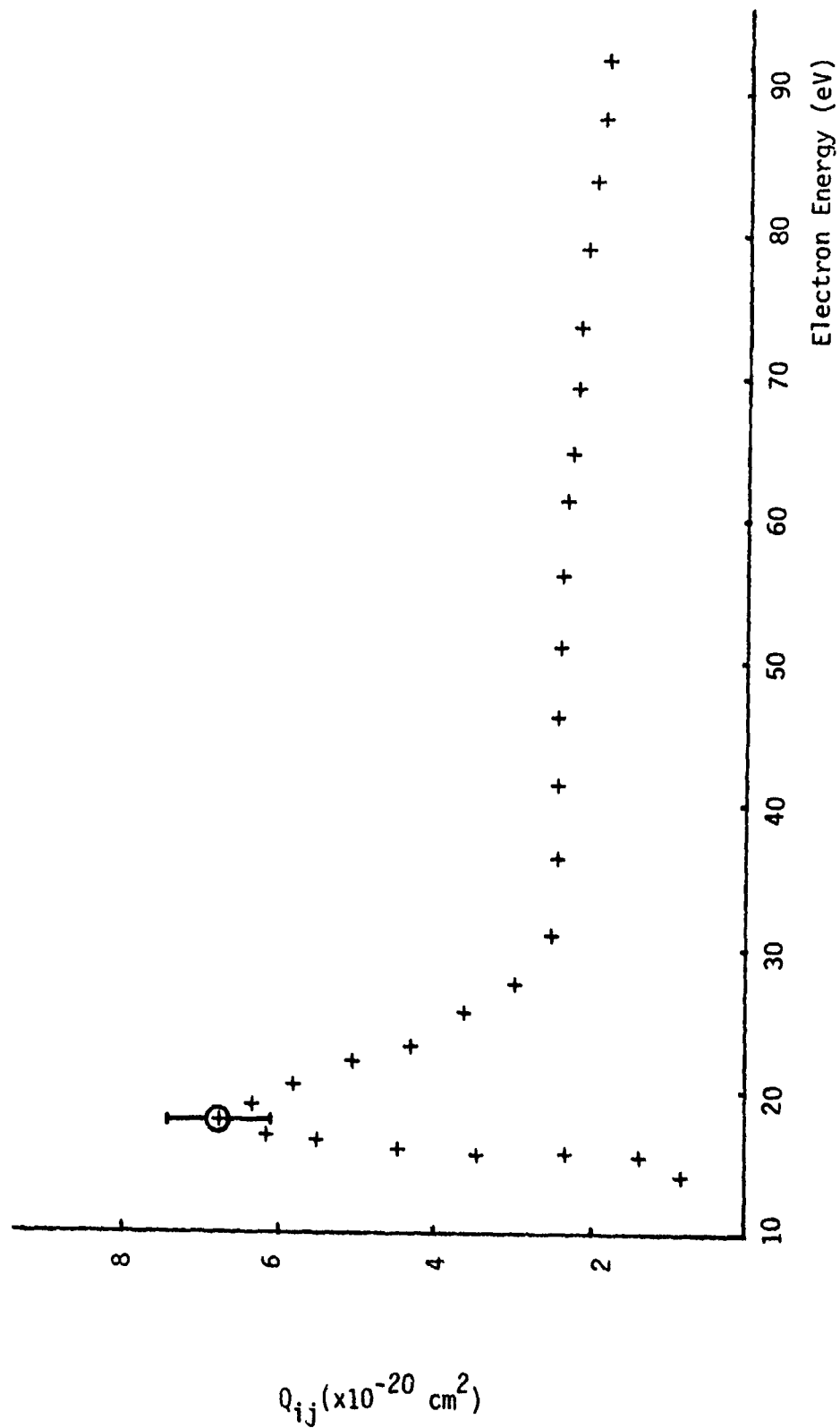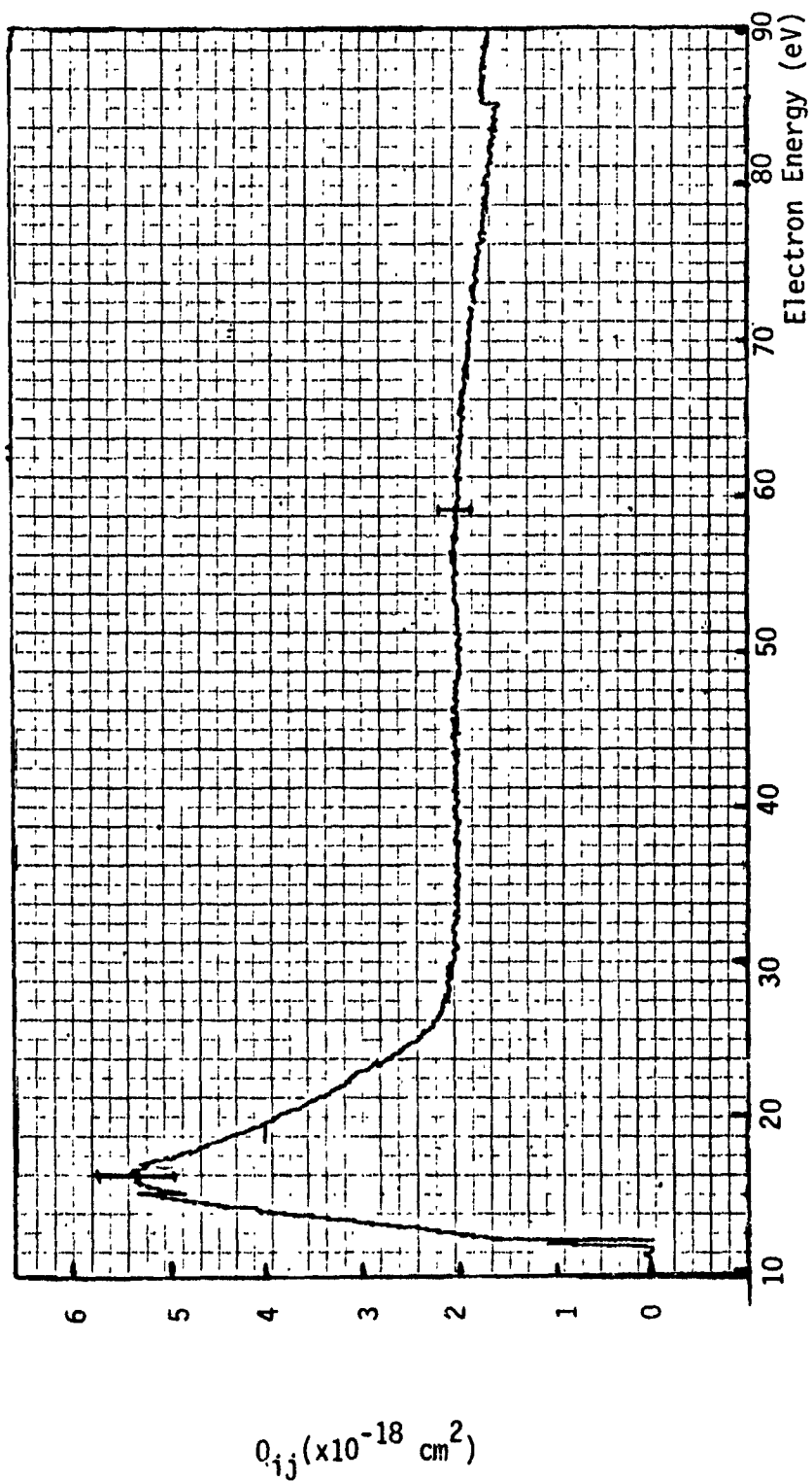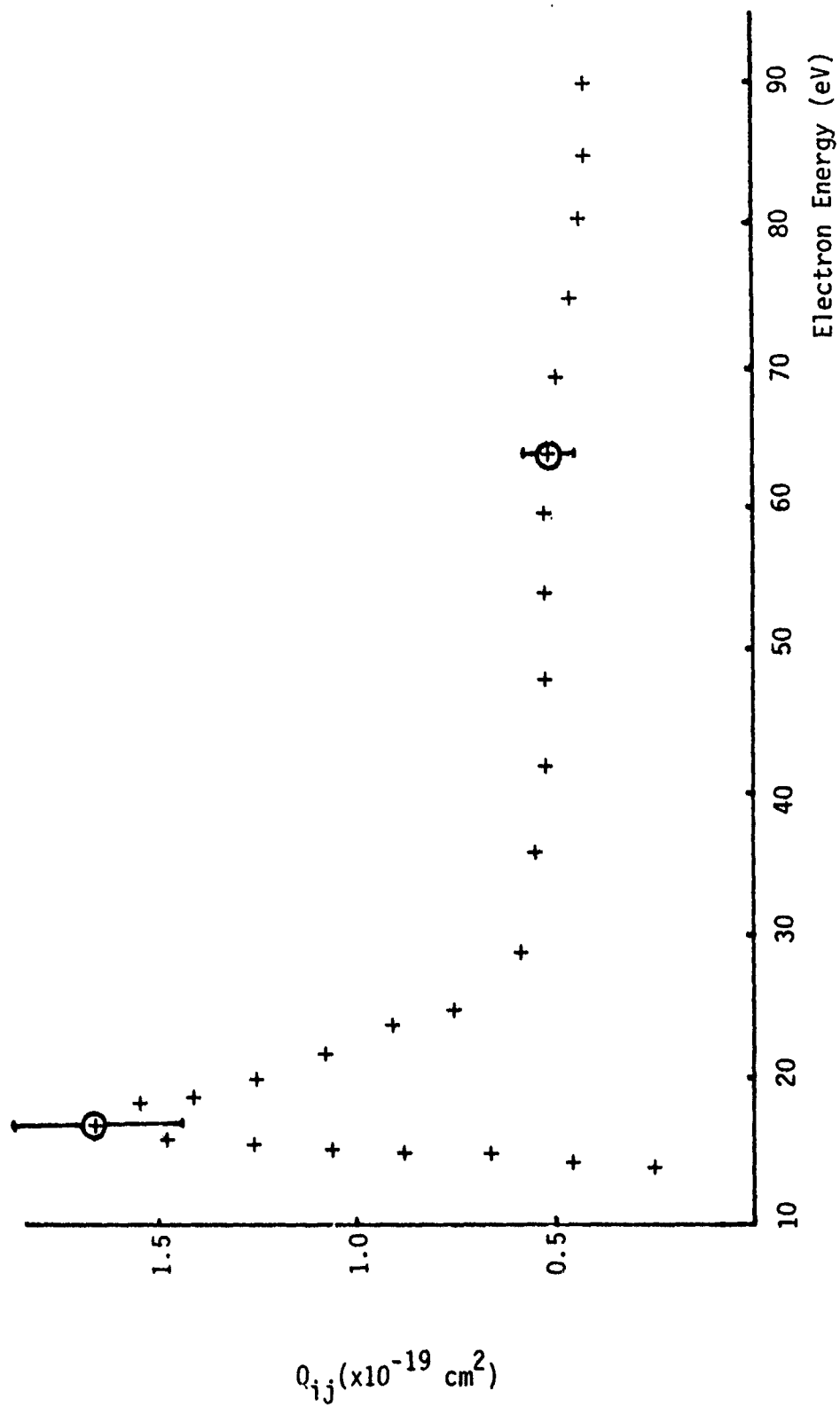
Figure 32.   Xe 4624 Å (7p[1½]→6s[1½]°)

$Q_{ij}(x10^{-19} cm^2)$
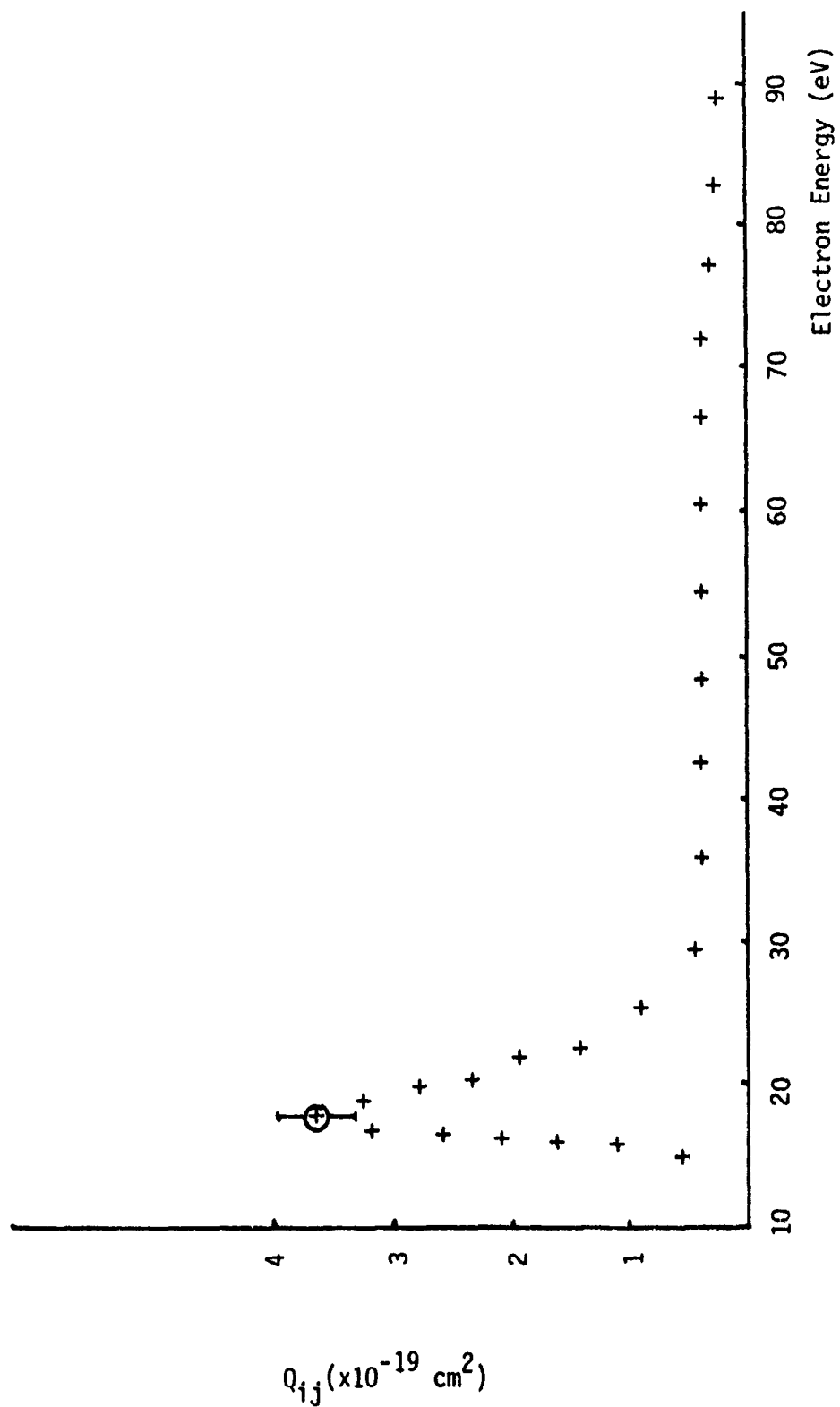
Figure 33. Xe 4671 Å ($7p[2\frac{1}{2}] \rightarrow 6s[1\frac{1}{2}]°$)

$Q_{ij}(\times 10^{-19} \text{ cm}^2)$

Electron Energy (eV)

52

Electron Energy (eV)

$Q_{ij}(\times 10^{-17}\ cm^2)$
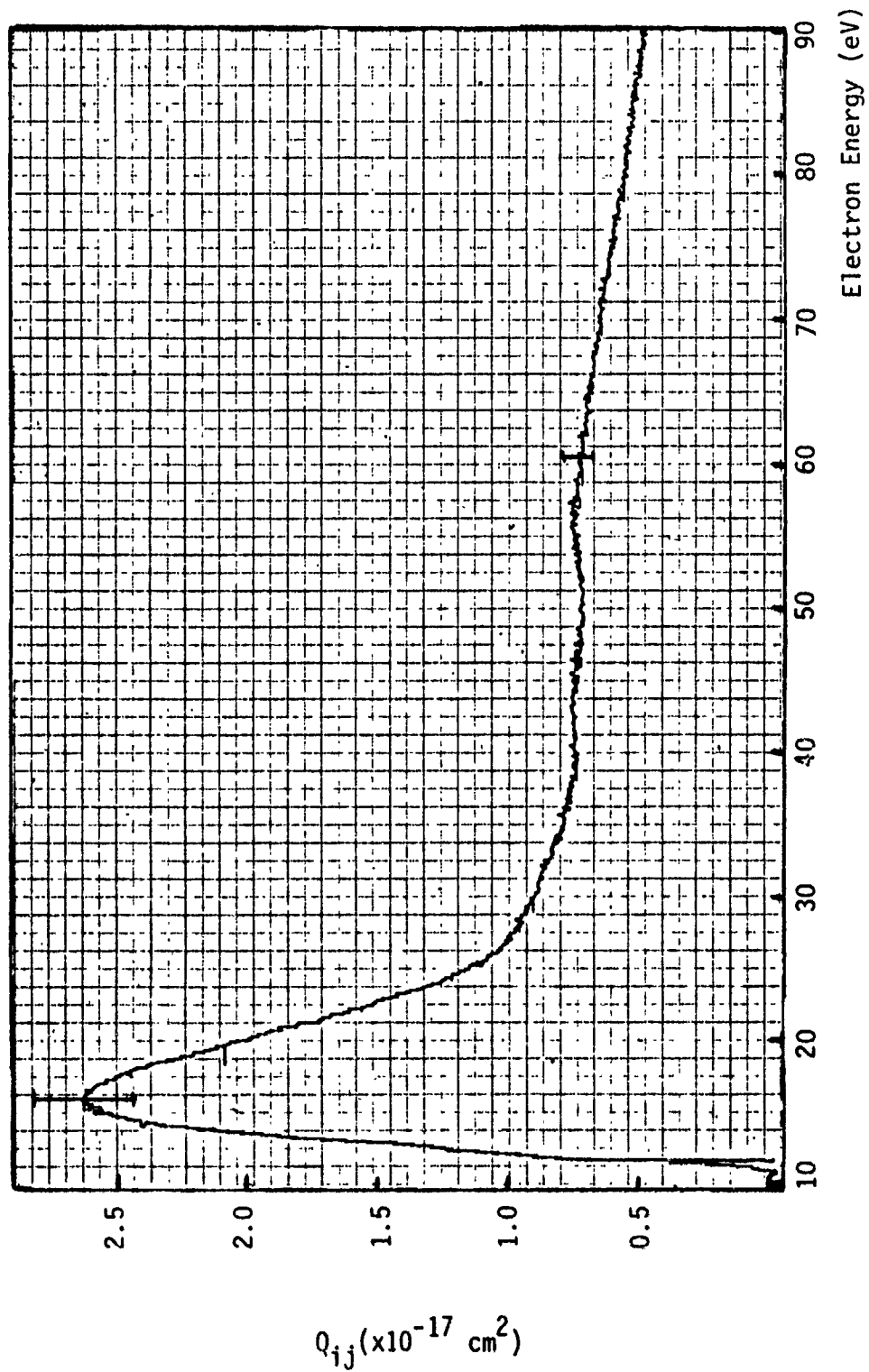
Figure 34.   Xe 8819 Å (6p[2½]→6s[1½]°)

53
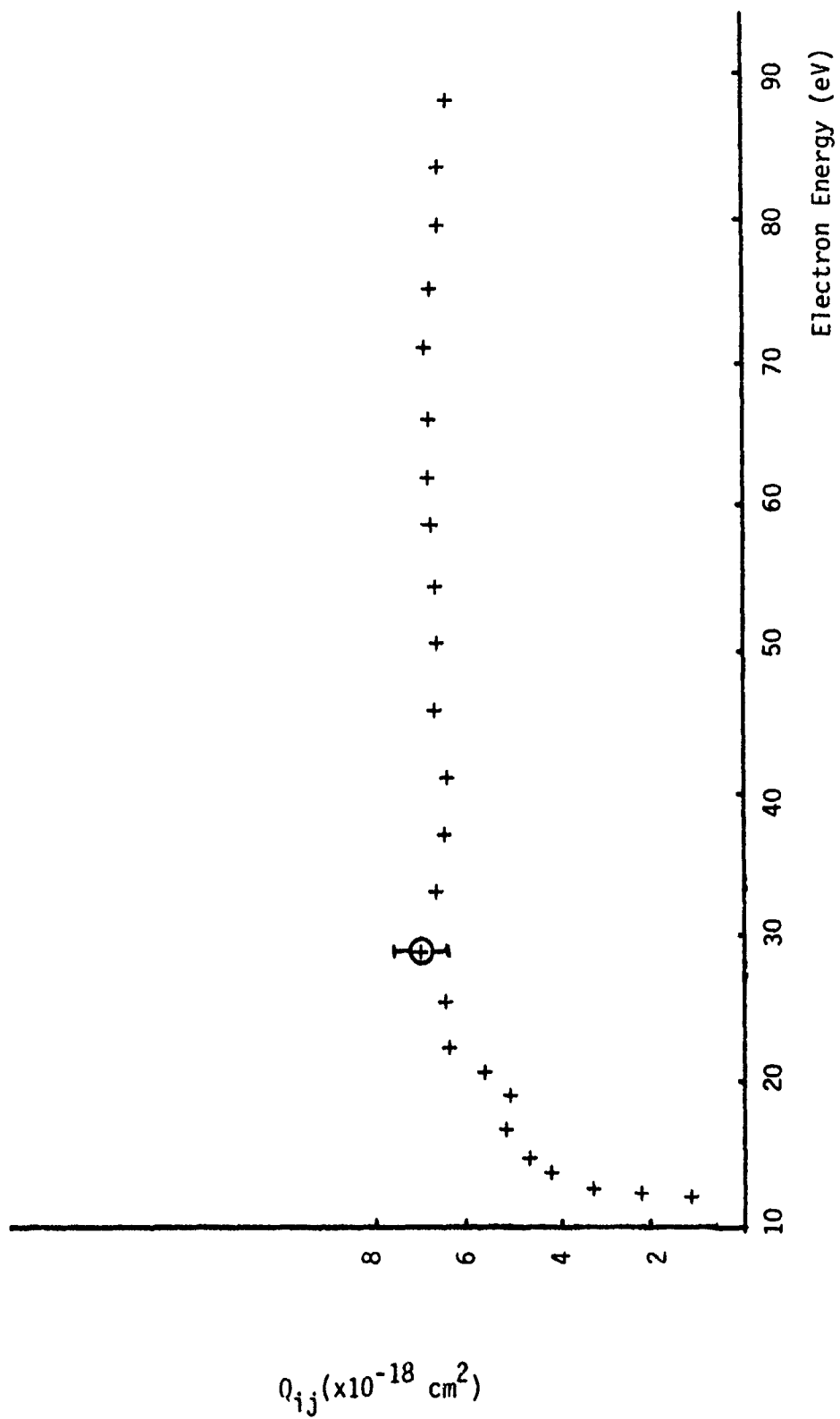
Figure 35.   Xe 8280 Å ($6p[\frac{1}{2}] \rightarrow 6s[1\frac{1}{2}]°$)

54

Figure 36.   Xe 7887 Å (6p'[½]→6s'[½]°)

Q_{ij}(x10^{-18} cm^2)

Electron Energy (eV)

55
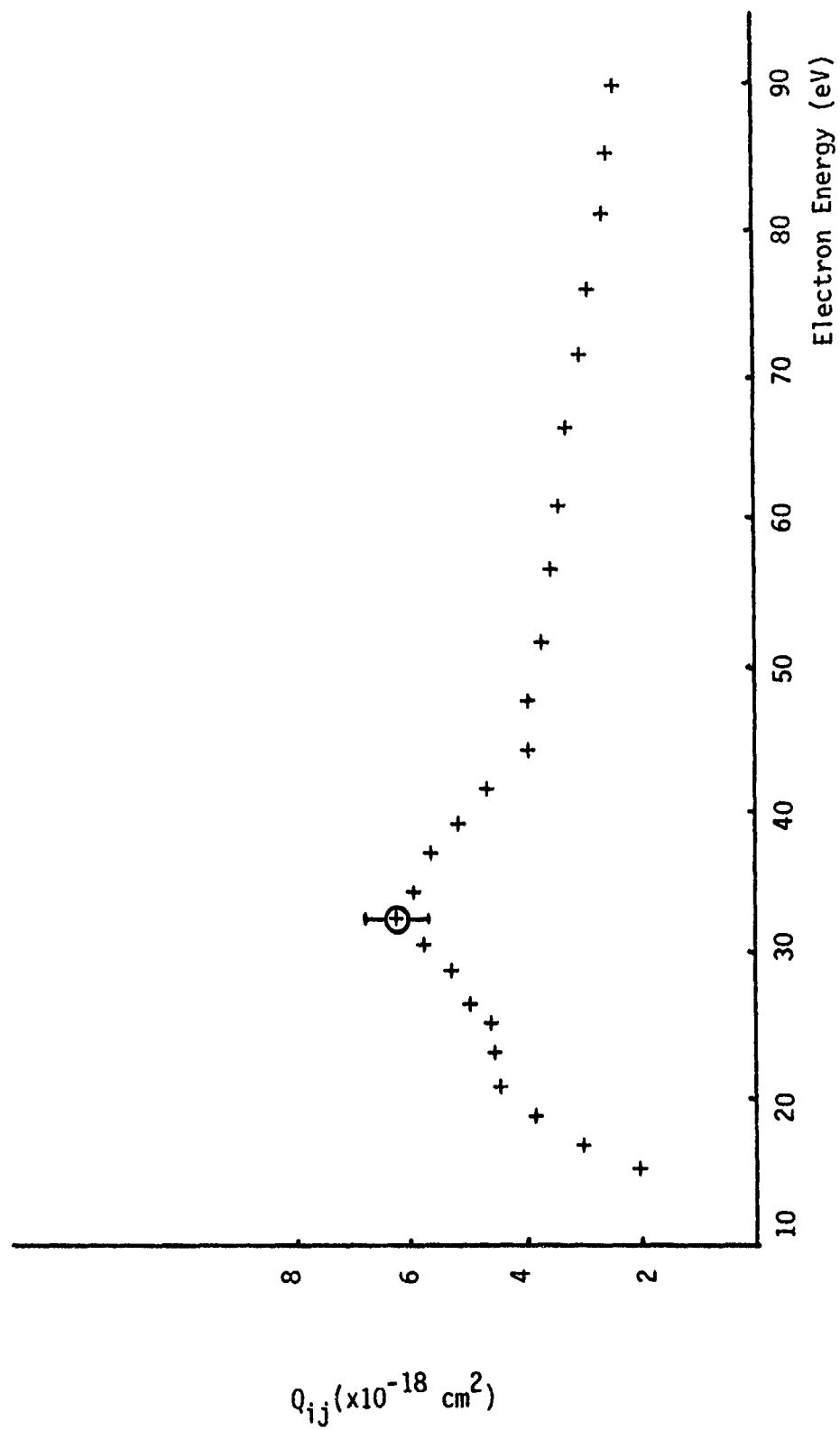
It is generally expected that transitions which are allowed by quantum mechanics selection rules will be more intense and have broader excitation functions than those transitions which are forbidden. The sharper excitation functions represent triplet transitions which are not allowed by quantum mechanics selection rules because a spin flip of one of the orbital electrons is required. A singlet transition which requires no spin flip is an allowed transition and, therefore, has a broader excitation function. However, heavier noble gases (i.e., krypton and xenon) have wavefunctions which are a combination of singlet and triplet basis functions. The shapes of these excitation functions depend upon the relative weights of the basis functions. It has been observed by Sharpton et. al (Ref. 23;1305) that in the case of neon, with a $2p^6$ ground state, that for a given configuration $2p^5n\ell$, the states with odd values of $J+1$ have larger cross sections than states with even values of $J+1$. The following observations are made for the present results for xenon. The transitions from the d levels show sharp peaks and large peak cross sections. The 5d' transitions have greater intensities than the transitions from the 8d level. The s level transitions appear to have more broadly peaked excitation functions and the peak cross sections are of average intensity compared to transitions from other levels.

The p levels seem to show both broad and sharp peaks in the excitation functions depending upon the value of the angular momentum J. The intensities of the p level transitions also vary according to the value of J. The intensities of the peak cross sections are shown in Appendix B. The transitions above the dotted line have sharply peaked excitation functions, while those below the line are broader. Those

56

transitions from upper excited levels with angular momentum values of one or two have peak cross sections which are weak. The lowest peak cross section was obtained from the 4501 $\overset{o}{A}$ transition from the 6p level with J=2. The value of the cross section for the transition is 3.79 x 10^{-20}. Transitions from upper p levels with J=0,3 appeared to have more intense peak cross sections. The strongest cross section was found in the 8819 $\overset{o}{A}$ transition from the 6p level which had a value of three for the angular momentum. The only discrepancy for these assumptions is for the intensity of the peak cross section for the 8231 $\overset{o}{A}$ transition which was much greater than that predicted. However, the double peak implies entrapment of resonance radiation and/or cascade overlap which tend to increase the intensity.

The pressures and electron gun energies used were sufficient to create xenon II lines in some cases. These lines result from ionization of the xenon gas atoms. In certain cases, the xenon II lines have wavelengths within 4 $\overset{o}{A}$ of the xenon I wavelengths. The xenon II lines have maximum cross sections at electron energies between 30 eV and 50 eV. If the monochromator slit is 400 microns wide, then these lines are unresolvable. The result on excitation functions for xenon I lines is a large "hump" with a maximum between 30 eV and 50 eV. This large "hump" has a threshhold which is approximately 26 eV, and therefore, is not obviously the result of cascading effects. Figure 37 shows this effect on the excitation function for the 4923 $\overset{o}{A}$ transition. The excitation function for the xenon I transition at 4843 $\overset{o}{A}$ also shows this effect as seen in Figure 38. Examination of spectral lines for xenion II transitions (Ref. 19:581) yields no evidence for a xenon II line at 4923$\pm$ 4 $\overset{o}{A}$,
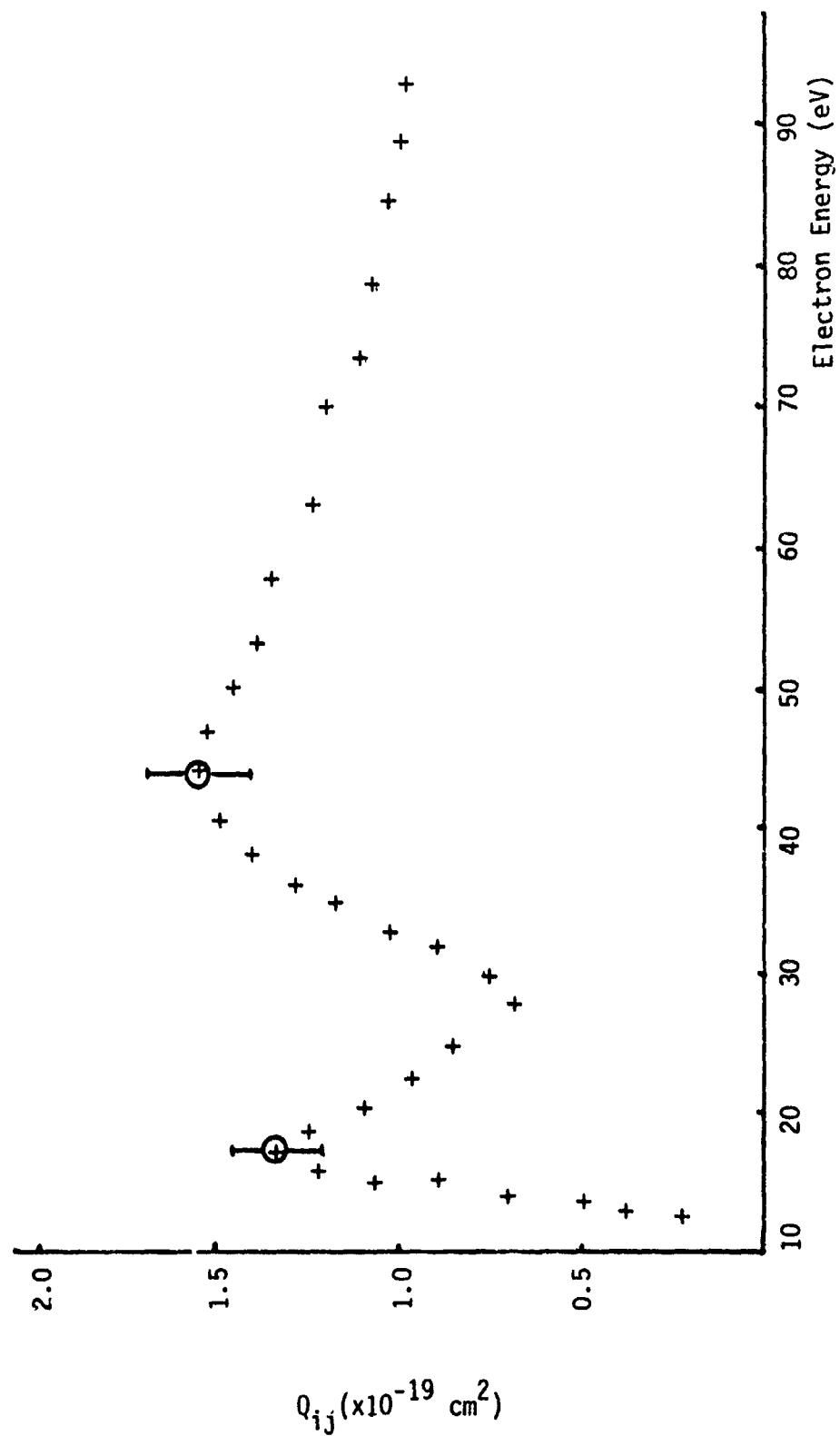
57

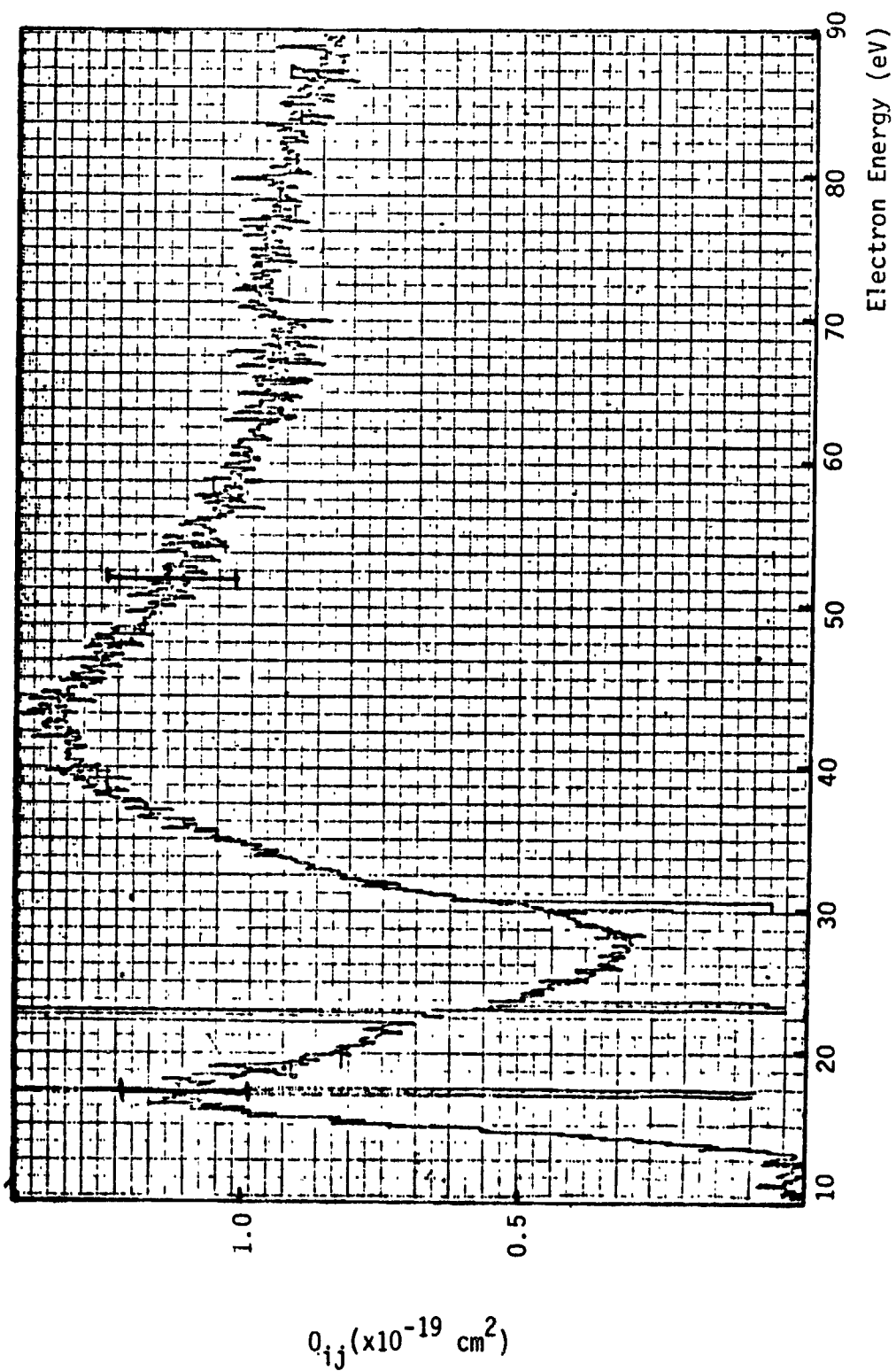Figure 37.   Xe 4923 Å and Unknown 4927 Å

58

Figure 38.   Xe 4843 $\overset{\circ}{A}$ and Xe$^+$ 4844 $\overset{\circ}{A}$

59

however, a xenon II line at 4844 Å does exist. Therefore, the double maximum on 4843 Å excitation function is evidently a result of observing two lines, a xenon I line and a xenon II line. The large "hump" for the 4923 Å transition appeared to be too large for cascading effects, so the monochromator slits were reduced to 150 microns and a spectrum was taken around 4923 Å at 45 eV. The results displayed in Figure 39 show an unidentified line at 4927 Å. These lines are separated by 1.64 Å at half maximum. The excitation functions for the 4923 Å and 4927 Å lines were examined using 150 micron slits. Figure 40 shows the excitation function for the 4923 Å line and Figure 41 gives the excitation function for the unidentified line at 4927 Å. Although the unidentified spectral line could be that of an impurity, no other evidence of impurities was discovered. In addition, the threshhold and characteristic shape of the excitation function for the 4927 Å line were similar to those of xenon II lines measured in this work. Therefore, this spectral line is presumed to be a previously unidentified xenon II line.

Other lines (i.e., 4670 Å and 4807 Å) have small "humps" which can be explained by cascading effects, but could also be a result of contributions from xenon II lines (i.e., 4672 Å and 4806 Å respectively). Figure 42 shows the excitation function for the 4843 Å transition, which is a xenon I transition. The shape of the xenon II transition is given in Figure 43 for 4844 Å. Most xenon II transitions have peak cross sections at electron energies around 40 eV.

Error Analysis

The error in the energy of the electrons is due to an energy spread in the electron distribution and a potential shift. The poten-

60
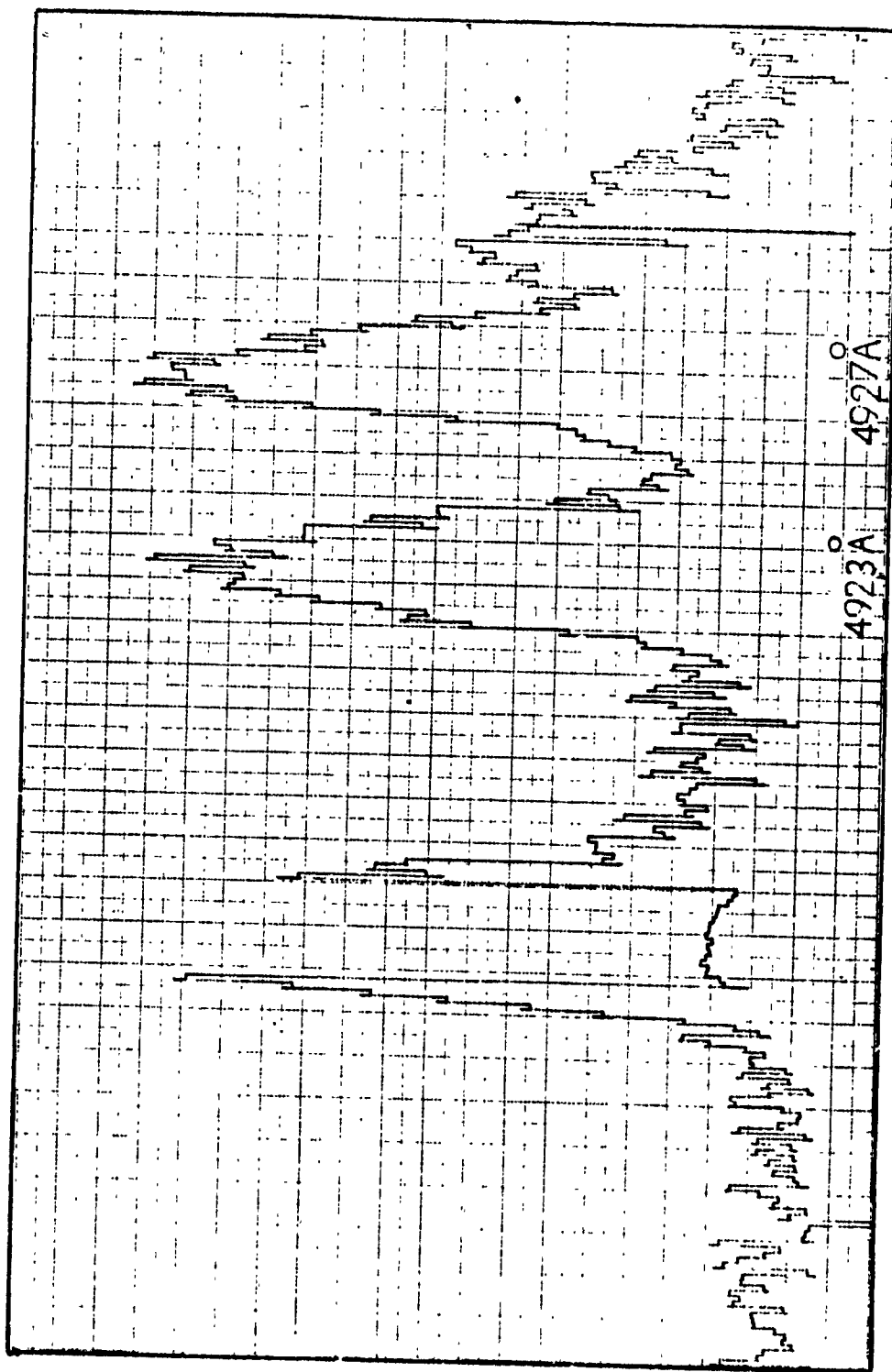
Figure 39.   Spectrum 4923 Å – 4927 Å

61

Electron Energy (eV)

$Q_{ij}(\times 10^{-19} \text{ cm}^2)$
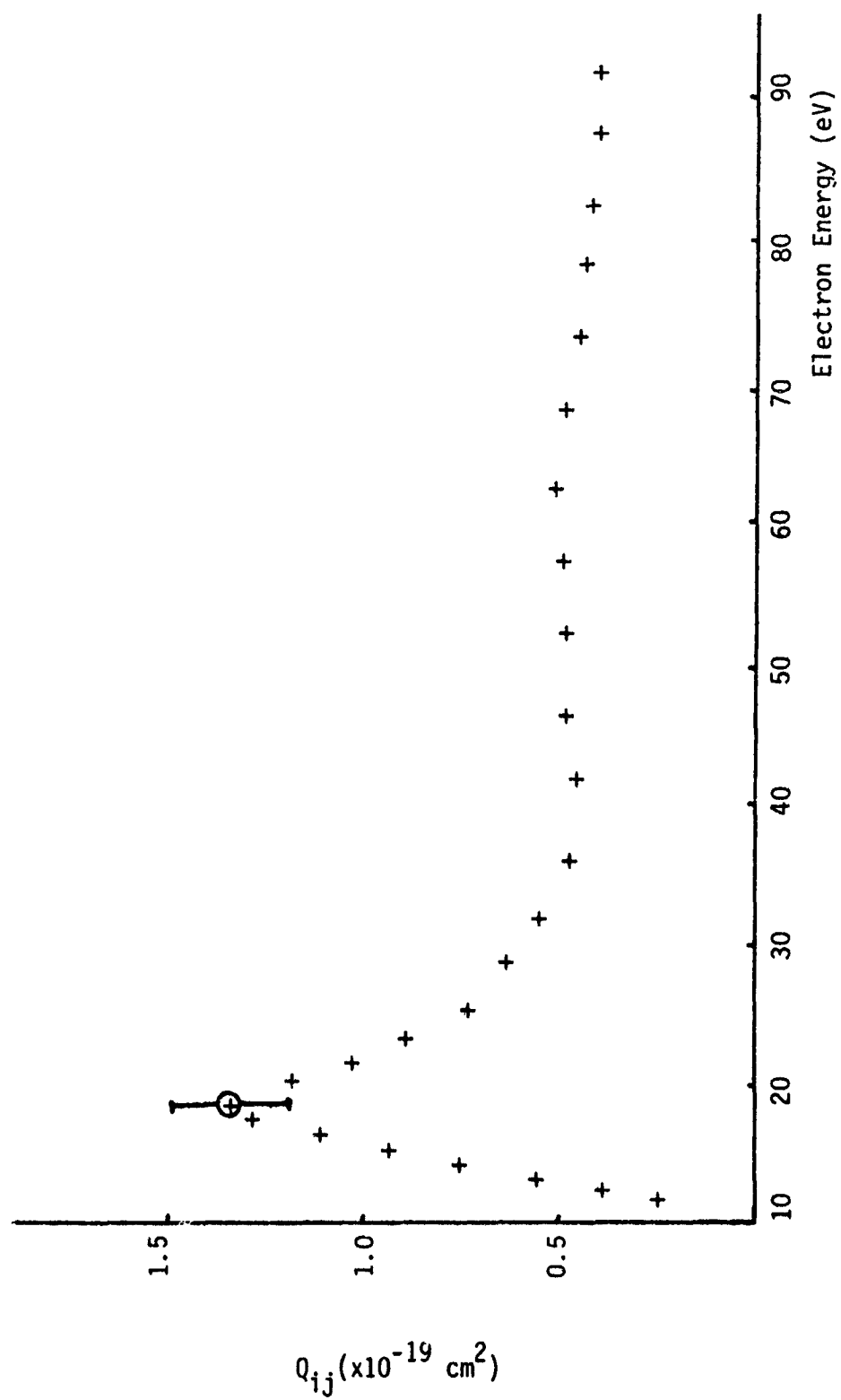
Figure 40.   Xe 4923 Å (7p[2½]→6s[1½]°)
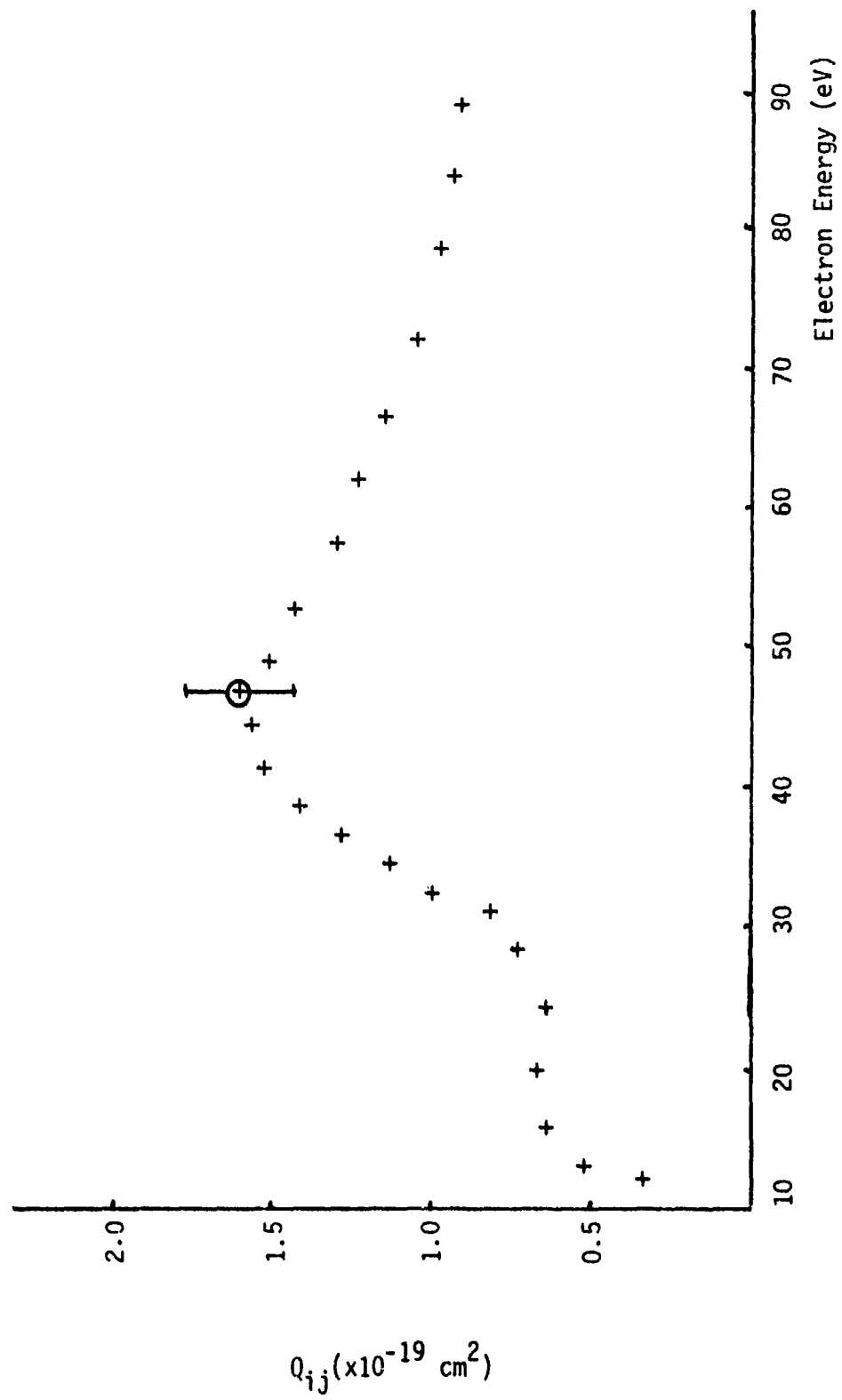
Figure 41. Unknown 4927 $\overset{\text{o}}{\text{A}}$

63
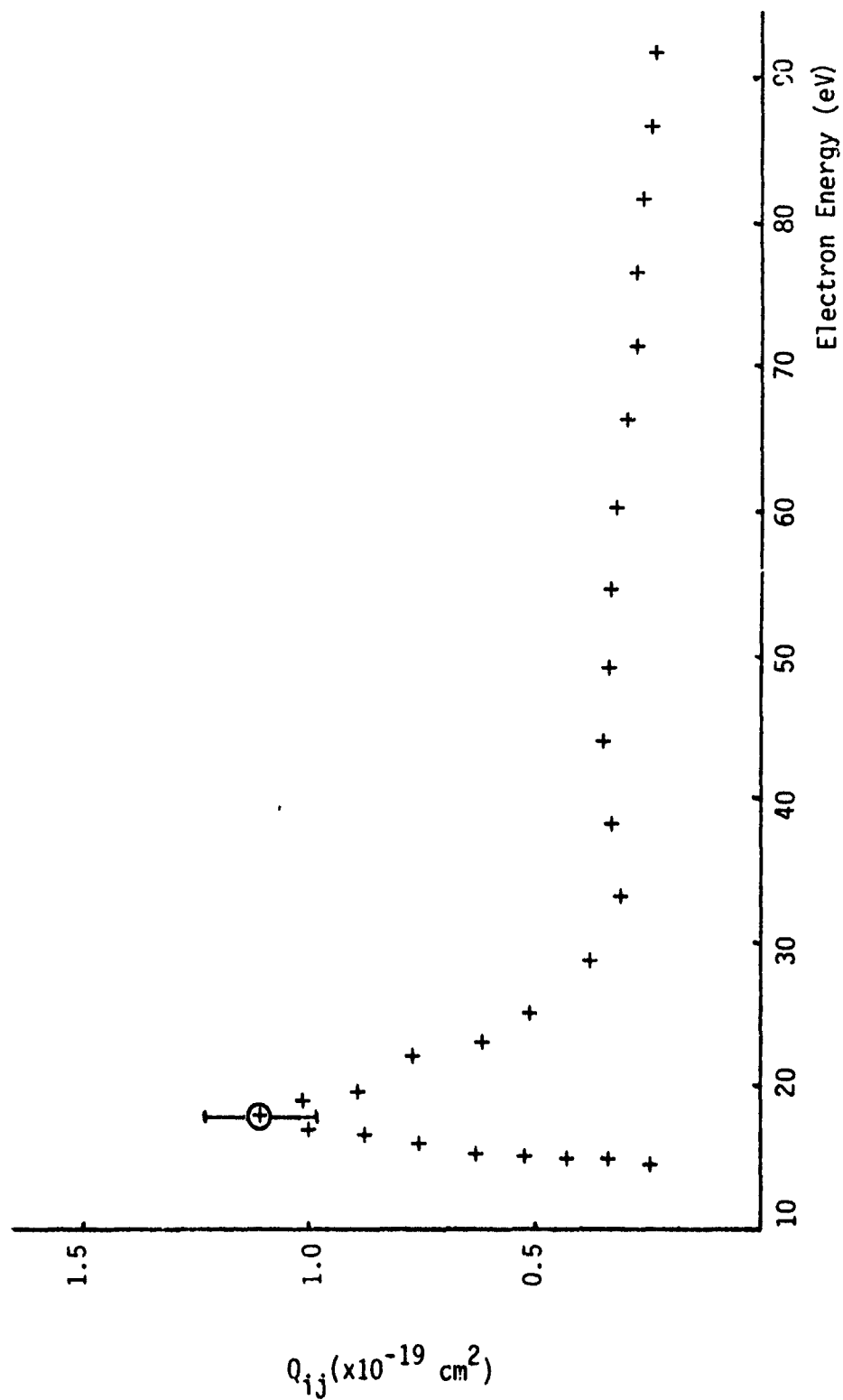
Figure 42. Xe 4843 Å ($7p[1\frac{1}{2}] \rightarrow 6s[1\frac{1}{2}]°$)

Q_{ij} ($\times 10^{-19}$ cm^2)

Electron Energy (eV)

64
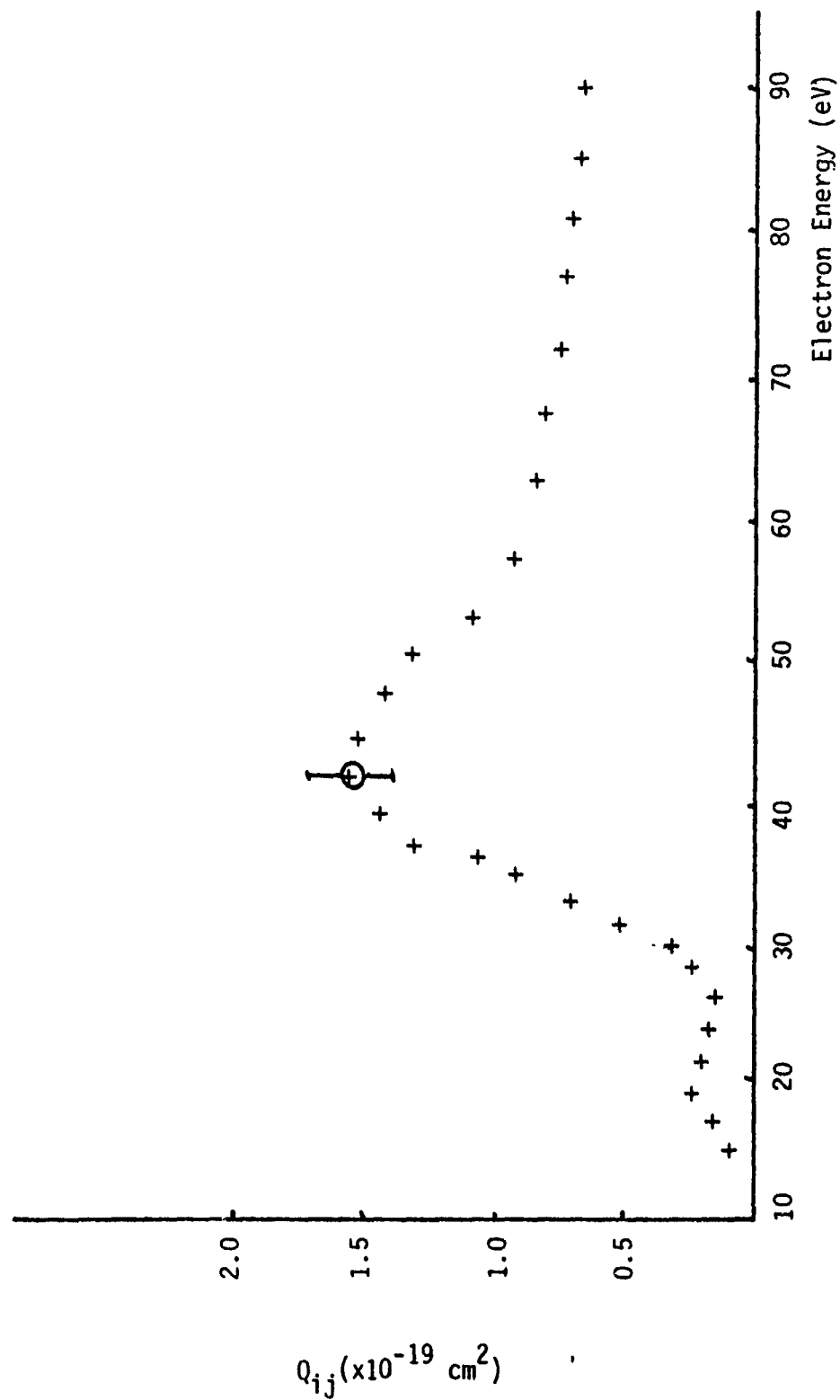
Figure 43. Xe$^+$ 4844 Å ($6p\,^4D^0-6s\,^4P$)

tial shift may be measured as the difference between the spectroscopic value for the onset of excitation and the observed value, and is correctable to 0.1 eV. The energy spread is approximately 1.5 eV at electron energies less than the ionization potential for xenon (12.1 eV). The energy spread increases to about 2.5 eV when an energy greater than that necessary for ionization is reached.

The governing equation for the cross section is given by Equation 15. The parameters which have non-varying errors are $\Omega(3\%)$, Δx (1%), $t(\lambda)$ (1%), and $S(\lambda)$ (2%). The error in the number density N may be determined by the gas law:

$$PV = NRT \tag{40}$$

The errors in the volume and temperature are 2% and 5% respectively. The error in the pressure arises from the calibration of the pressure gauge, the distance of the gauge from the interaction volume, and a slight gas flow through the interaction region. A combination of these errors gives an error in pressure up to 5%. Therefore, the error in the number density is 7%. The parameters which very significantly and thus have varying errors are the signal I_c and the electron current I. The signal has statistical deviation which varies from 1% to 11% depending upon the intensity of the signal and the noise level for the particular day of measurement. The highest percentage error was noticed in Figure 29 for the 4501 $\overset{o}{A}$ transition, where the error was 17% at the peak cross section and 15% at the cross section for 70 eV. The lowest error was obtained in Figure 34 for the 8819 $\overset{o}{A}$ transition, where the error was 8% for the peak cross section and 9% for the cross section at 60 eV. Error bars are used to show the possible error in all excitation

66

functions. In those instances where the error varies more than 2% over the entire energy range, error bars are displayed for the peak cross section and a cross section at a higher electron energy (usually 60-70 eV).

The shapes and peak intensities of the excitation functions obtained in this work were compared, where applicable, to those obtained by P. V. Felstan and I. P. Zapesochnyi (Ref. 24). The shapes were comparable and the peak intensities were within the percentage errors outlined in this paper. The discrepancies between this work and previous results probably arise from the use of improved instrumentation and the resulting improvements in signal strength and spectral resolution.

Recommendations

Further studies should be made on static operation of barium implanted cathodes. Techniques (i.e., appendage pumps) should be improved to prevent contamination of the cathode from residual oxygen.

Cascading effects on high intensity laser lines should be investigated. The cascading transitions and their relative cross sections should be determined for various electron energies between zero and 100 eV.

High resolution should be obtained for the purpose of identifying previously unresolvable lines and cascading transitions which result in "humps" or double peak excitation functions.

Bibliography

1. Lake, Max L. _Experimental Measurements of Cumulative Excitation and Ionization in Atomic and Molecular Gases_. Dayton, Ohio, Universal Energy Systems, Inc., December 1977.

2. Vidal, C. R. (to be published), 1967.

3. Lake, Max L. Vice President, Universal Energy Systems (private communication). WPAFB, Ohio, June 18, 1979.

4. Walker, Keith G. _Simultaneous Ionization and Excitation of Neon by Electron Collision_. Norman, Oklahoma, University of Oklahoma, 1971.

5. DeJoseph, Charles A. Research Scientist, Universal Energy Systems, Inc. (private communication). WPAFB, Ohio, June 20, 1979.

6. Vansickle, Cliff. Research Scientist, Universal Energy Systems, Inc. (private communication). WPAFB, Ohio, July 29, 1979.

7. Crawford, C. K. _Electron Impact Ionization Cross Section_. AMRL-TR-67-376. WPAFB, Ohio, Air Force Material Lab, December, 1967.

8. Fox, R. E., _et al_. "Ionization Potentials and Probabilities Using Mass Spectrometry," _Physical Reviews_, 84, 859-860 (1951).

9. Cloutier, G. G. and H. I. Schiff. _Advances in Mass Spectrometry_, edited by J. D. Waldron. New York: Pergamon Press, 1959.

10. Bletzinger, Peter. Physicist, Air Force Aero Propulsion Lab (private communication). WPAFB, Ohio, August 21, 1979.

11. Zapesochnyi, I. P. and P. V. Felstan. "Excitation of Inert Gases in Electron-Atom Collisions," _Ukr. Fiz ZH_, 11:1197 (1965).

12. Lees, J. H. "The Excitation Function of Helium," _Proceedings of the Royal Society of London Ser A_, 137:173 (1932).

13. Miller, F. L. _Excitation of Helium Atoms by Electron Impact_, Thesis. University of Oklahoma, 1964.

14. Moustafa Moussa, H. R. _Excitation of Helium by Fast Electrons and Polarization of the Resulting Radiation_, Thesis. University of Leiden, 1967.

15. Kieffer, L. J. _Compilation of Low Energy Electron Collision Cross Section Data_. JILA Information Center Report No. 7, line and level excitation. Boulder, Colorado, University of Colorado, Sept. 1969.

16. Sharpton, Francis A. _Excitation of Neon Atoms by Electron Impact._ Norman, Oklahoma, University of Oklahoma, 1968.

17. St. John, R. M. "Calibration of a Spectroscopic System," _Methods of Experimental Physics_, 8:27 (1969).

18. Jobe, J. D. _Excitation Processes in Helium._ A Ph.D. dissertation. Norman, University of Oklahoma, 1968.

19. Striganov, A. R. and N. S. Sventitski. _Tables of Spectral Lines of Neutral and Ionized Atoms_, New York. IFI/Plenum, 1968.

20. Rostovikova, G. S., _et al._ "Measurements of Cross Section for Excitation of Xenon Lines by Electron Impact," _Opt. Spektrosk_, 34: 3-5 (January 1973).

21. H. S. W. Massey and E. H. S. Burhop. _Electronic and Ionic Impact Phenomena_, second edition, 1. Oxford: Oxford University Press, 1969.

22. Racah, Giulio. "On a New Type of Vector Coupling in Complex Spectra," _Physical Review_, 61: 537 (2 March 1942).

23. Sharpton, Francis A., _et al._ "Experimental and Theoretical Studies of Electron-Impact Excitation of Neon," _Physical Review A_, 2:1305-1321 (October 1970).

24. Felstan, P. V. and I. P. Zapesochnyi. "Excitation of Inert Gases at Electron-Atom Collisions," _Ukr Fiz ZH_, 13:205-210 (1968).

APPENDICES

APPENDIX A

START UP/SHUT DOWN PROCEDURE

Once the pressure in the system has reached 10^{-7} torr range, the electron gun can be activated. Current is applied to the heater filament in increments of 50 milliamps every 15 minutes until a heater current of 1 amp was reached. The electron gun will be outgassing in this range and, therefore, the cooling system for the gun must not be turned on until outgassing is completed. If the cooling system were on, then the impurities would accumulate on the coldest portions of the copper shield and tubing. Once one amp current has been reached, the pressure should be approximately 1×10^{-7} torr and stable; which indicates that outgassing is completed.

The heater current was then increased in increments of 100 milliamps every 15 minutes until an operating current of approximately 4.50 amps was reached. Electron current was first detected at 4.00 amps of heater current.

Once the electron gun had been activated, gas was allowed to flow into the system until the pressure reached 1×10^{-4} torr. The gate valve was then closed and the interaction volume was sealed off by closing the gold seal and butterfly values.

The detection system then needed to be turned on. First, the cooling to the PMT was set at $-20^{\circ}C$. The room lights were then turned off, and the PMT amplifiers were turned on. The PMT was operated at a total divider potential of 1500 V. The photon counter was then set to display the signal at one count per second. The signal was fed into

the Y-axis of the X-Y recorder after being divided by the current. The electron energy was plotted on the X-axis and was swept at 0.1 eV/sec. The monochromator was tuned to a specific wavelength and the X-Y recorder plotted the excitation function.

| $\overset{o}{(\text{A})}$	Transition	J	$Q_{ij}(\text{cm}^2)$
4697	$7p[\tfrac{1}{2}] \rightarrow 6s[1\tfrac{1}{2}]°$	$2 \rightarrow 2$	9.60×10^{-20}
7336	$5d'[2\tfrac{1}{2}]° \rightarrow 6s[2\tfrac{1}{2}]°$	$3 \rightarrow 2$	2.83×10^{-18}
6318	$8d[3\tfrac{1}{2}]° \rightarrow 6p[2\tfrac{1}{2}]°$	$4 \rightarrow 3$	5.42×10^{-19}
4830	$7p[2\tfrac{1}{2}]° \rightarrow 6s[1\tfrac{1}{2}]°$	$1 \rightarrow 1$	1.21×10^{-19}
4501	$6p'[\tfrac{1}{2}] \rightarrow 6s[1\tfrac{1}{2}]°$	$2 \rightarrow 1$	3.79×10^{-20}
4734	$6p'[1\tfrac{1}{2}] \rightarrow 6s[1\tfrac{1}{2}]°$	$2 \rightarrow 1$	6.56×10^{-20}
8231	$6p[1\tfrac{1}{2}] \rightarrow 6s[1\tfrac{1}{2}]°$	$2 \rightarrow 2$	5.46×10^{-18}
4624	$7p[1\tfrac{1}{2}] \rightarrow 6s[1\tfrac{1}{2}]°$	$2 \rightarrow 2$	1.66×10^{-19}
4671	$7p[2\tfrac{1}{2}] \rightarrow 6s[1\tfrac{1}{2}]°$	$3 \rightarrow 2$	3.60×10^{-19}
8819	$6p[2\tfrac{1}{2}] \rightarrow 6s[1\tfrac{1}{2}]°$	$3 \rightarrow 2$	2.67×10^{-17}
4923	$7p[2\tfrac{1}{2}] \rightarrow 6s[1\tfrac{1}{2}]°$	$2 \rightarrow 1$	1.34×10^{-19}
4843	$7p[1\tfrac{1}{2}] \rightarrow 6s[1\tfrac{1}{2}]°$	$2 \rightarrow 1$	1.11×10^{-19}
7803	$8s[1\tfrac{1}{2}]° \rightarrow 6p[2\tfrac{1}{2}]°$	$1 \rightarrow 2$	3.38×10^{-19}
8576	$7p[\tfrac{1}{2}] \rightarrow 6s'[\tfrac{1}{2}]°$	$0 \rightarrow 1$	2.80×10^{-19}
4807	$7p[\tfrac{1}{2}] \rightarrow 6s[1\tfrac{1}{2}]°$	$0 \rightarrow 1$	1.23×10^{-19}
8280	$6p[\tfrac{1}{2}] \rightarrow 6s[1\tfrac{1}{2}]°$	$0 \rightarrow 1$	6.88×10^{-18}
7887	$6p'[\tfrac{1}{2}] \rightarrow 6s'[\tfrac{1}{2}]°$	$0 \rightarrow 1$	6.21×10^{-18}
4844	$6p\,^4D° \rightarrow 6s\,^4P$	$7/2 \rightarrow 5/2$	1.55×10^{-19}

APPENDIX C

PHOTOGRAPHS OF ELECTRON GUN

4 in.
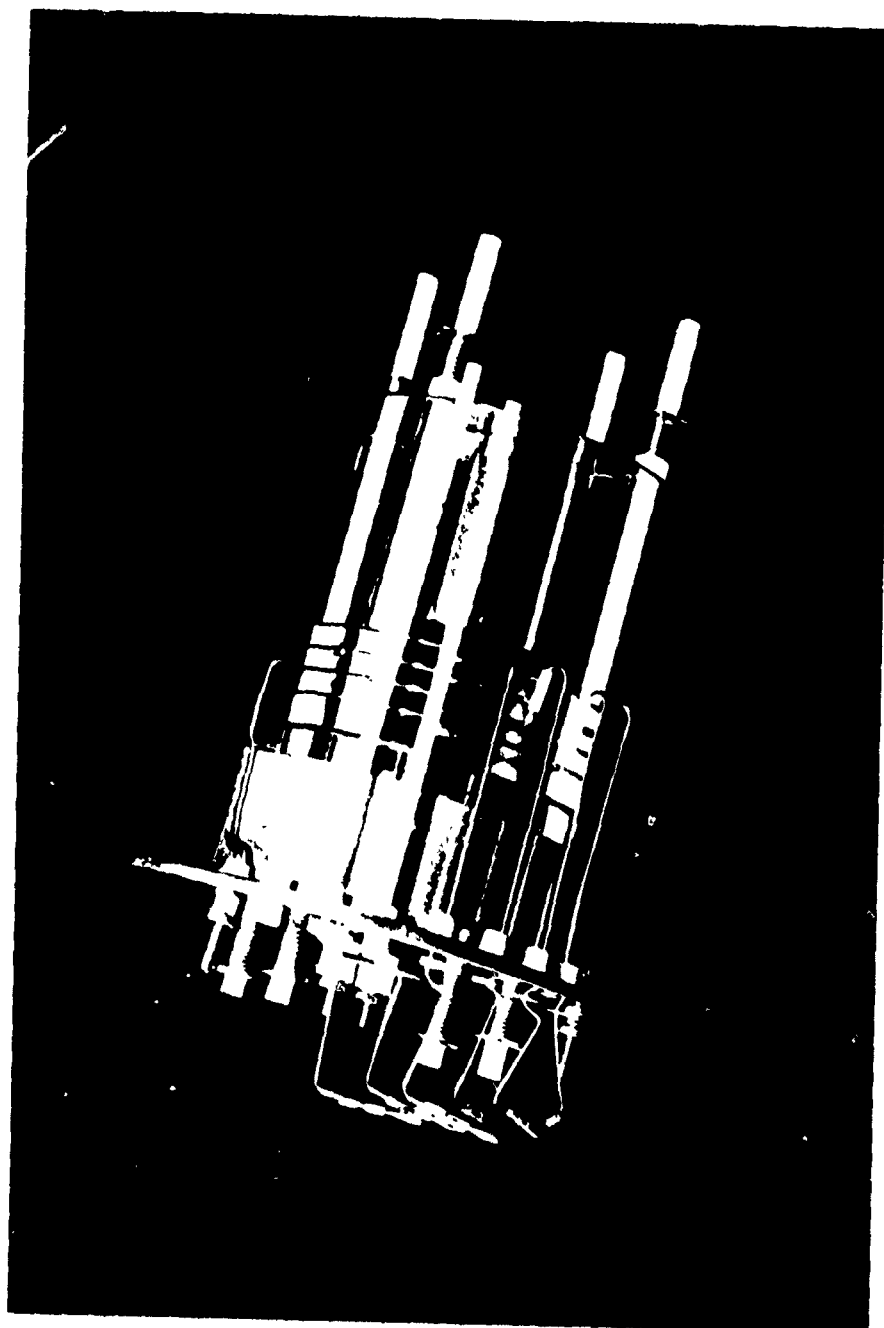
Electron Gun

8 in.
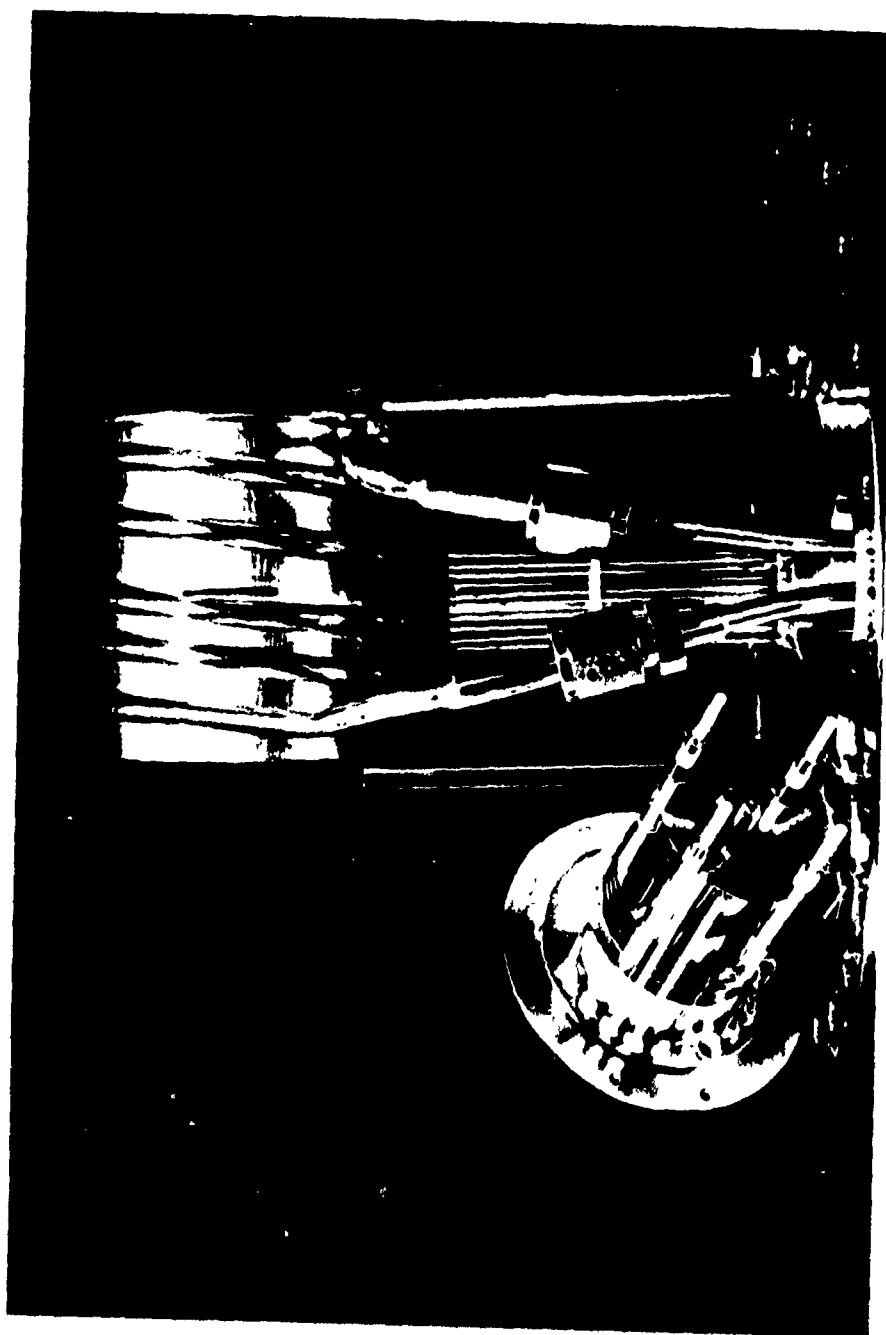
Electron Gun Shield

Vita

      Mark Douglas Stephen was born in Castle A.F.B., California on 24 April 1956. He graduated from Summerville High School in Summerville, South Carolina on 31 May, 1974. While attending college, he joined Air Force ROTC and was commissioned on 12 May 1978. He graduated the following day from the University of South Carolina with a Bachelor's Degree in Physics. His first active duty assignment was to the Air Force Institute of Technology at Wright-Patterson A.F.B., Ohio.

                                    Permanent Address: 280 Orange Street
                                                             Darlington, S.C.
                                                                29532

REPORT DOCUMENTATION PAGE		READ INSTRUCTIONS BEFORE COMPLETING FORM
1. REPORT NUMBER AFIT/GEP/PH/79D-11	2. GOVT ACCESSION NO.	3. RECIPIENT'S CATALOG NUMBER
4. TITLE *(and Subtitle)* MEASUREMENTS ON ELECTRON IMPACT EXCITATION FUNCTIONS OF XENON TRANSITIONS		5. TYPE OF REPORT & PERIOD COVERED M.S. THESIS
		6. PERFORMING ORG. REPORT NUMBER
7. AUTHOR(s) MARK D. STEPHEN 2d Lt USAF		8. CONTRACT OR GRANT NUMBER(s)
9. PERFORMING ORGANIZATION NAME AND ADDRESS Air Force Institute of Technology (AFIT-EN) Wright-Patterson AFB OH 45433		10. PROGRAM ELEMENT, PROJECT, TASK AREA & WORK UNIT NUMBERS
11. CONTROLLING OFFICE NAME AND ADDRESS Air Force Aero Propulsion Laboratory (AFAPL/POE-3) Wright-Patterson AFB OH 45433		12. REPORT DATE December 1979
		13. NUMBER OF PAGES 89
14. MONITORING AGENCY NAME & ADDRESS*(if different from Controlling Office)*		15. SECURITY CLASS. *(of this report)* UNCLASSIFIED
		15a. DECLASSIFICATION/DOWNGRADING SCHEDULE

16. DISTRIBUTION STATEMENT *(of this Report)*

Approved for Public Release; Distribution Unlimited.

17. DISTRIBUTION STATEMENT *(of the abstract entered in Block 20, if different from Report)*

18. SUPPLEMENTARY NOTES   Approved for public release; IAW AFR 190-17

JOSEPH P. HIPPS, Major, USAF
Director of Public Affairs

19. KEY WORDS *(Continue on reverse side if necessary and identify by block number)*

Cross Section	Excitation Function
Xenon	Electron Impact

20. ABSTRACT *(Continue on reverse side if necessary and identify by block number)*

Electron impact excitation functions have been measured in xenon for excitation of some of the 6p, 6p´, 7p´, 8s, 5d´, and 8d levels.   A one centimeter diameter electron beam was used to excite the gas atoms. The beam was made nearly mono-energetic by use of the retarding-potential-difference method. Most of the xenon I excitation functions were sharply peaked around 18 eV. Broader excitation functions were measured which had peak cross sections at electron energies around 30 eV. Cascading from higher energy

BLOCK 20 (Cont'd)

levels showed significant effects on selected optical excitation functions. The electron gun produced a current of approximately one milliamp. Measurement of some xenon II excitation functions produced by simultaneous ionization/excitation were obtained. The xenon II excitation functions demonstrated a maximum at approximately 35 eV, and a broader shape than the Xe I excitation functions.